Reactive nitrogen around the Arabian Peninsula and in the Mediterranean Sea during the 2017 AQABA ship campaign.

Nils Friedrich[1], Philipp Eger[1], Justin Shenolikar[1], Nicolas Sobanski[1], Jan Schuladen[1], Dirk Dienhart[1], Bettina Hottmann[1], Ivan Tadic[1], Horst Fischer[1], Monica Martinez[1], Roland Rohloff[1], Sebastian Tauer[1], Hartwig Harder[1], Eva Y. Pfannerstill[1], Nijing Wang[1], Jonathan Williams[1], James Brooks[2], Frank Drewnick[3], Hang Su[4], Guo Li[5], Yafang Cheng[5], Jos Lelieveld[1], John N. Crowley[1]

[1]Atmospheric Chemistry Department, Max Planck Institute for Chemistry, Mainz, 55118, Germany
[2]Centre for Atmospheric Science, University of Manchester, Manchester, M13 9PL, UK
[3]Particle Chemistry Department, Max Planck Institute for Chemistry, Mainz, 55118, Germany
[4]Multiphase Chemistry Department, Max Planck Institute for Chemistry, Mainz, 55118, Germany
[5]Minerva Research Group, Max Planck Institute for Chemistry, Mainz, 55118, Germany

Correspondence to: John N. Crowley (john.crowley@mpic.de)

Abstract. We present ship-borne measurements of NO_x ($\equiv NO + NO_2$) and NO_y ($\equiv NO_x$ + gas- and particle-phase organic and inorganic oxides of nitrogen) in summer 2017 as part of the expedition "Air Quality and climate change in the Arabian Basin" (AQABA). The NO_x and NO_z ($\equiv NO_y - NO_x$) measurements, made with a thermal dissociation cavity-ringdown-spectrometer (TD-CRDS), were used to examine the chemical mechanisms involved in the processing of primary NO_x emissions and their influence on the NO_y budget in chemically distinct marine environments, including the Mediterranean Sea, the Red Sea, and the Arabian Gulf which were influenced to varying extents by emissions from shipping and oil and gas production. Complementing the TD-CRDS measurements, NO and NO_2 data sets from a chemiluminescence detector (CLD) were used in the analysis. In all regions, we find that NO_x is strongly connected to ship emissions, both via direct emission of NO and via the formation of HONO and its subsequent photolytic conversion to NO. The role of HONO was assessed by calculating the NO_x production rate from its photolysis. Mean NO_2 lifetimes were 3.9 hours in the Mediterranean Sea, 4.0 hours in the Arabian Gulf and 5.0 hours in the Red Sea area. The cumulative loss of NO_2 during the night (reaction with O_3) was more important than daytime losses (reaction with OH) over the Arabian Gulf (by a factor 2.8) and over the Red Sea (factor 2.9), whereas over the Mediterranean Sea, where OH levels were high, daytime losses dominated (factor 2.5). Regional ozone production efficiencies (OPE; calculated from the correlation between O_x and NO_z, where $O_x = O_3 + NO_2$) ranged from 10.5 ± 0.9 to 19.1 ± 1.1. This metric quantifies the relative strength of photochemical O_3 production from NO_x, compared to the competing sequestering into NO_z species. The largest values were found over the Arabian Gulf, consistent with high levels of O_3 found in that region (10 – 90 percentiles range: 23-108 ppbv). The fractional contribution of individual NO_z species to NO_y exhibited a large regional variability, with HNO_3 generally the dominant component (on average 33 % of NO_y) with significant contributions from organic nitrates (11 %) and particulate nitrates in the PM_1 size range (8 %).

1 Introduction

35   The nitrogen oxides NO and NO_2 are emitted into the atmosphere in several natural and anthropogenic processes including lightning (Chameides et al., 1977; Lange et al., 2001), combustion (Lenner, 1987) and bacterial action in soil (Oertel et al., 2016). Due to their rapid interconversion, NO and NO_2 are often treated as a single chemical family (NO_x).

  The chemical processing of NO_x in the atmosphere, initiated by ozone and the radicals OH, HO_2 and NO_3, leads to the formation of NO_z (NO_z = HNO_3 + NO_3 + 2 N_2O_5 + RO_2NO_2 + $RONO_2$ + $XONO_2$ + XNO_2 + particulate nitrates) where R is

40   an organic fragment and X represents a halogen atom or an H-atom. The sum of NO_x and NO_z is referred to as total reactive nitrogen NO_y (Logan, 1983), which does not include N_2, N_2O, NH_3 or HCN.

  OH, formed e.g. via the photolysis of O_3 in the presence of water (reaction R1a and R1b) can directly convert both NO and NO_2 to more oxidised, acidic forms (R2, R3; where M is a collision partner). NO_x can be reformed from HONO at daytime through photolysis, with a noontime lifetime of ca. 20-30 minutes (Stutz et al., 2000).

$O_3 + h\nu$	$\rightarrow$	$O(^1D) + O_2$	(R1a)
$O(^1D) + H_2O$	$\rightarrow$	2 OH	(R1b)
$OH + NO + M$	$\rightarrow$	$HONO + M$	(R2)
$OH + NO_2 + M$	$\rightarrow$	$HNO_3 + M$	(R3)

  OH can also react with volatile organic compounds (VOCs) to generate peroxy radicals (RO_2, reaction R4). Reaction with

50   organic peroxy radicals converts NO to NO_2 (major channel; reaction R5a) or to organic nitrates $RONO_2$ (minor channel; reaction R5b), and sequesters NO_2 as peroxy nitrates RO_2NO_2 (reaction R7).

$OH + RH\ (+O_2)$	$\rightarrow$	$RO_2 + H_2O$	(R4)
$RO_2 + NO$	$\rightarrow$	$RO + NO_2$	(R5a)
$RO_2 + NO + M$	$\rightarrow$	$RONO_2 + M$	(R5b)
$HO_2 + NO$	$\rightarrow$	$OH + NO_2$	(R6)
$RO_2 + NO_2 + M$	$\rightarrow$	$RO_2NO_2 + M$	(R7)

55

  The formation of long-lived organic nitrates (R5b) and especially nitric acid (R3) represent daytime sinks for both NO_x and RO_x ($OH + HO_2 + RO + RO_2$).

  At nighttime, when the photolysis of NO_2 ceases, NO is sequentially converted to the NO_3 radical (R8). This radical can also

60   be a source of $RONO_2$ species through the addition to unsaturated VOCs. NO_3 exists in thermal equilibrium with NO_2 and N_2O_5 (R9) and the heterogeneous loss of N_2O_5 to aqueous surfaces results in transfer of NO_y to the particle phase as HNO_3 (R10) or its loss via deposition. In some (especially marine) environments (Osthoff et al., 2008; Kercher et al., 2009), loss of N_2O_5 to particles can result in formation of $ClNO_2$ (R11) which, via photolysis, reforms NO_2 the next day.

$NO_2 + O_3$	$\rightarrow$	$NO_3 + O_2$	(R8)
65 $NO_3 + NO_2 + M$	$\rightleftharpoons$	$N_2O_5 + M$	(R9)
$N_2O_5 + H_2O$	$\rightarrow$	2 HNO_3	(R10)

$$N_2O_5 + Cl^- \qquad \rightarrow \qquad ClNO_2 + NO_3^- \hspace{4cm} (R11)$$

The above reactions illustrate that NO_x and VOCs provide the catalyst and fuel for photochemical ozone formation, the efficiency of which is determined by the competition between photolysis of NO_2 to ozone and its conversion to NO_z (Day et al., 2003; Wild et al., 2014; Wild et al., 2016; Womack et al., 2017). Modelling studies have identified the Arabian Gulf as a hotspot for O_3 pollution and photochemical smog, with O_3 mixing ratios exceeding 100 ppbv (Lelieveld et al., 2009).

The lack of measurements in the Arabian Gulf and the Eastern Mediterranean, both of which are expected to be significantly impacted by climate change (Lelieveld et al., 2012), preclude accurate prognosis of air-quality in these regions and provide the rationale for conducting the AQABA campaign (AQABA: Air Quality and climate change in the Arabian BAsin), in which a large suite of instruments were operated in regions that were influenced by anthropogenic emissions from megacities, petrochemical and shipping activity as well as desert dust emissions and through regions that could be classified as maritime background. Emissions from oil exploration provide a complex atmospheric mixture of NO_x and anthropogenic VOCs. The presence of desert dust can have a significant impact on the budget of inorganic acids such as HNO_3. Finally, the overall elevated temperatures and actinic fluxes on AQABA promote rapid photochemical processing of NO_x. We therefore expect a more varied and complex chemistry than found in remote marine locations.

Previous analyses from this campaign focussed on sources and sinks of non-methane hydrocarbons (Bourtsoukidis et al., 2019), the role of OH reactivity in ozone chemistry (Pfannerstill et al., 2019), formation of $ClNO_2$ (Eger et al., 2019a), ethane and propane emissions from the Red Sea (Bourtsoukidis et al., 2020), emission factors in ship plumes (Celik et al., 2020), marine emissions of methane sulfonamide (Edtbauer et al., 2020), rates of net O_3 production (Tadic et al., 2020), and the abundance of carbonyl compounds.

In this paper we present NO_x, NO_y and NO_z mixing ratios obtained by a thermal dissociation cavity-ringdown-spectrometer (TD-CRDS), together with NO and NO_2 mixing ratios from a chemiluminescence detector, a comprehensive set of ancillary measurements and an analysis of the results in terms of photochemical processing/aging of air masses, chemical sources of NO_x (e.g. from the photolysis of HONO), and the efficiency of ozone formation.

The ozone production efficiency (OPE), a metric used in the analysis of the O_3 formation, quantifies the fractional transformation of primarily emitted NO_x to O_3 (Liu et al., 1987; Trainer et al., 1993) and thus reflects the relative importance of competing photochemical processes leading to O_3 and NO_z formation from NO_x. High values of OPE are favoured by low OH and VOC concentrations and values exceeding 80 have been reported for remote marine environments. Low, single digit values have been observed in polluted urban environments (Rickard et al., 2002; Wang et al., 2018). The location-dependence of the OPE can be further classified with previous observations from the literature. Minimal OPEs in urban environments between 1 and 2 have been reported from the Beijing area (Lin et al., 2011; Ge et al., 2013) and from the USA (Daum et al., 2000; Sillman, 2000; Nunnermacker et al., 2004). In rural and suburban environments, the OPE can increase to values between 10 and 15, as demonstrated in Northern America (Olszyna et al., 1994; Roussel et al., 1996; Fried et al., 1997; Ninneman et al., 2017) and in China (Sun et al., 2010). From oceanic samples, OPEs of 65 and 87 were observed on the south-eastern coast of the UK (Rickard et al., 2002) and on Sable Island, Canada (Wang et al., 1996). Flights over the Western Pacific Ocean

found values of 102-246 in the tropical area (latitude 0-18 °N), and of 73-209 further north (18-42 °N) (Davis et al., 1996). For the AQABA campaign, we expect lower OPEs than those observed in remote oceanic locations, due to the variable influx from harbours, coastal pollution and surrounding ship traffic.

2 Methods

105 The AQABA ship campaign followed a route from Toulon in Southern France to Kuwait (and back) via the Mediterranean Sea, the Suez Canal, the Red Sea, the Arabian Sea and the Arabian Gulf (see Fig. 1). Stops were made in Malta, Jeddah, Djibouti and Fujairah on the first leg (24 June to 30 July 2017), and in Fujairah and Malta on the second leg (2 August to 30 August 2017). Most measurements started in the south-eastern Mediterranean Sea on the first leg and finished ca. half-way between Sicily and Corsica on the second leg. The instruments were located either in air-conditioned research containers

110 aboard, or directly on the deck of the 73 m long research vessel "*Kommandor Iona*". Periods during which instrument inlets were contaminated by ship-stack emissions from the ship (identified based on relative wind direction and speed, and the variability in measured SO_2 and NO mixing ratios) were excluded from the analysis. This resulted in rejection of 38.4 % of the data points on the first leg, when the wind and ship direction were often similar, and rejection of 1.4 % on the second leg of the campaign, when sailing mainly into the wind.

2.1 TD-CRDS instrument for NO_x, NO_y and NO_z detection

115

The TD-CRDS instrument, its operating principles and laboratory characterisation, and a validation of the NO_x measurements versus an independent CLD instrument have recently been presented (Friedrich et al., 2020). The TD-CRDS (located in an air-conditioned research container on the front deck of the vessel) has two separate cavities operating at a wavelength of 405 nm and at sub-ambient pressure (720 to 770 hPa) to prevent condensation of water in inlet lines under humid conditions. One of

120 the cavities is connected to an inlet (PFA tubing) at ambient temperature, the other cavity is connected to a tubular quartz inlet, heated to 850 °C to thermally dissociate NO_y trace-gases to NO or NO_2. The TD-oven was accommodated in an aluminium box on top of the container with the inlet ca. 1.2 m above the container roof. Air samples reached the TD area less than 30 cm behind the tip of the inlet and we expect negligible inlet losses for NO_y species. Inlet lines of the heated and the ambient temperature channel were each overall ca. 4 m long (2 m located inside and 2 m outside the container).In the Red Sea and

125 Arabian Gulf, the inlet heating of the NO_y channel was switched off occasionally during the hottest hours of the day, to prevent damage to the oven electronics. The campaign data coverage for NO_y is 65 %, considering only time periods when the ship was moving.

The total uncertainty (at 50 % relative humidity and one minute integration time) amounts to 11 % + 10 pptv for NO_x and to 16 % + 14 pptv for NO_z if we disregard the non-quantitative detection of coarse-mode, non-refractory nitrate (see below).

130 Detection limits (5 s integration time) during the AQABA campaign were 98 pptv for NO_x, 51 pptv for NO_y, and 110 pptv for NO_z and are higher than those reported for laboratory operation owing to problems with optical alignment due to the motion

of the ship. Detection limits are defined as the 2σ standard deviation between consecutive zeroing periods. Under laboratory conditions, NO_x detection limits of 40 pptv (1 min average) were obtained (Friedrich et al., 2020); 6 pptv (40 s) have been achieved with undegraded mirrors (Thieser et al., 2016).

135 The NO_z mixing ratios obtained using the TD-CRDS were calculated from the difference between NO_y and NO_x measurements and thus contain a contribution from particulate nitrate. Friedrich et al. (2020) have shown that this instrument measures ammonium nitrate quantitatively, but detects only a fraction (≈ 25 %) of sodium nitrate ($NaNO_3$) of 200-300 nm diameter as NO_x. The inefficient detection of some non-refractory nitrate species (e.g. $NaNO_3$) means that the NO_y mixing ratios presented below are thus (potentially) lower limits. As $NaNO_3$ is usually associated with coarse-mode aerosol (particle diameter $> 1\mu m$)

140 this also implies that the particle-phase nitrate measured by the TD-CRDS is comparable to that measured by an Aerosol Mass Spectrometer (HR-TOF-AMS, see Sect. 2.3). In marine environments, sea salt aerosol can be the dominant aerosol component (Lewis and Schwartz, 2004). We therefore note that the definition of NO_y, in this work, is restricted to non-refractory nitrate particles which can be vaporised by the AMS or in the TD inlet of the CRDS. Nitrate detection by the AMS is further discussed in Sections 3.2.2 and 3.4.

145 High loadings of coarse mode particles are associated with high wind speeds, which were encountered on the first leg passing the Strait of Bab al-Mandab, through the Arabian Sea and until the Gulf of Oman, and on the second leg in the Arabian Sea and in the Northern Red Sea. The fractional contribution of coarse-mode particles to the overall mass concentration were derived using data from an Optical Particle Counter (OPC) and via the $(PM_{10}-PM_1)/PM_{10}$ ratio (both PM_1 and PM_{10} were measured with the OPC). We see from Fig. S1 that the impact of coarse mode nitrate may have been largest on both legs in

150 the transitional area between Southern Red Sea and Arabian Sea, where OPC PM_{10} mass concentrations exceeded 150 $\mu g\ m^{-3}$ and the coarse mode fraction was consistently $>$ ca. 90 %.

2.2 CLD measurements of NO_x

NO and NO_2 were measured with a chemiluminescence detector (CLD 790 SR, ECO Physics, 5 s time resolution) as described in Tadic et al. (2020), with total measurement uncertainties of 6 % (NO) and 23 % (NO_2) and detection limits of 22 pptv for

155 NO and 52 pptv for NO_2, both calculated at a time resolution of 5 s and a confidence interval of 2σ. The CLD detection method is based on the chemiluminescence of electronically excited NO_2^* formed in the reaction of NO with O_3. Ambient NO_2 is photolytically converted to NO by exposure to UV light from LEDs emitting at wavelengths close to 398 nm. The CLD was calibrated every six hours using a 2 ppmv NO gas standard.

2.3 Other measurements

160 An overview of the instruments deployed is given in Table 1. Total organic nitrates (ONs) were measured as the sum of peroxy nitrates (PNs, RO_2NO_2) and alkyl nitrates (ANs, $RONO_2$) in a five channel, thermal dissociation cavity-ring-down spectrometer (5C-TD-CRDS, Sobanski et al. (2016)). SO_2 and $ClNO_2$ were measured with a Chemical Ionisation Quadrupole Mass Spectrometer (CI-QMS) with 15 s time resolution (Eger et al., 2019a; Eger et al., 2019b). The detection limit for SO_2

and ClNO$_2$ were 38 pptv and 12 pptv, the total uncertainties were 20 % ± 23 pptv (SO$_2$) and 30 % ± 6 pptv (ClNO$_2$). Particulate phase nitrate (pNit) and sulphate concentrations in the PM$_1$ size range were obtained by an Aerosol Mass Spectrometer (Aerodyne HR-ToF-AMS; DeCarlo et al. (2006)) with measurement uncertainties of 30 % and 35 %, respectively for the mass concentrations of NO$_3^-$ and SO$_4^{2-}$. Total aerosol mass concentrations in the PM$_1$ and PM$_{10}$ size ranges were calculated from particle size distributions, detected with an optical particle counter (OPC, Grimm model 1.109; size range: 250 nm to 32 µm) in a 6 s time resolution and with a 35 % uncertainty. Ozone was measured by optical absorption at 253.65 nm in a commercial ozone monitor (2B Technologies Model 202) with total measurement uncertainty of 2 % ± 1 ppbv and a detection limit of 3 ppbv (at 10 s integration time). HONO mixing ratios were measured by a long path absorption photometer (LOPAP; Heland et al. (2001)) with a 3-5 pptv detection limit and a measurement uncertainty of 20 %. The path length of the instrument was 1.9 m, and the inlet was also located on the foredeck of the ship in ca. 5 m distance to the TD-CRDS inlets. A spectral radiometer (Metcon GmbH) measured wavelength resolved actinic flux, which was converted to photolysis rate constants (J) for NO$_2$, NO$_3$ and HONO using evaluated quantum yields and cross sections (Burkholder et al., 2015). The overall uncertainty in J is ca. 15 %, which includes calibration accuracy (Bohn et al., 2008) and the neglect of upwelling radiation from the sea-surface. OH concentrations were obtained from a custom-built laser induced fluorescence instrument (LIF) (Martinez et al., 2010; Regelin et al., 2013)) with an upper limit total uncertainty of 40 %. Total OH reactivity measurements were performed according to the comparative reactivity method (Sinha et al., 2008), with a 5 minute detection limit of 5.4 s^{-1} and a ca. 50 % total uncertainty, as described in Pfannerstill et al. (2019). HCHO was detected by a commercial instrument (AL4021, AERO-LASER GmbH) according to the Hantzsch method, and had a relative uncertainty of 13 % (Stickler et al., 2006). Multi-pass absorption spectroscopy using a quantum-cascade-laser was used to measure CO mixing ratios with 20 % uncertainty, and a limit of detection of 0.6 ppbv (Li et al., 2013).

2.4 Meteorological data

Temperature, wind direction, wind speed and relative humidity were measured by a weather station (Neptune, Sterela), together with the GPS position and velocity of the ship. Back trajectories were obtained using the HYSPLIT transport and dispersion model (Stein et al., 2015; Rolph et al., 2017). The trajectories were calculated backwards for 48 hours from the GPS location of the ship with a starting height of 100 m AMSL, using the Global Data Assimilation System (GDAS1) meteorological model. The back trajectories were limited to 48 hours as this exceeds the lifetimes of both NO$_x$ and NO$_z$ (see later) and is thus sufficient to indicate potential source regions. Back trajectories displayed in graphs are considered to be representative for the prevailing atmospheric flow conditions when passing the respective areas along the AQABA ship track.

3 Results and discussion

In Fig. S2 we show the complete NO$_x$, NO$_y$ and NO$_z$ time series from the campaign, averaged from the 5 s raw data time resolution onto a 5 min grid. Periods of contamination by the ship's own exhaust are indicated by grey background colouring.

The regional variation in NO_x and NO_z during the 2nd leg is illustrated in Fig. S3c and Fig. 1 which also delineates the campaign into the "Red Sea" (2-16 July 2017 and 17-24 August 2017), the "Arabian Sea" (16-24 July 2017 and 7-17 August 2017), the "Arabian Gulf" (24-31 July 2017 and 3-7 August 2017), and the "Mediterranean Sea" (24-31 August 2017).

Altogether, 4.8 % of the NO_x measurements during AQABA were below the ca. 100 ppt detection limit of the TD-CRDS instrument, indicating only sporadic occurrence of maritime background conditions. Similar observations were made by Tadic et al. (2020), with only 3.3 % of the NO_x dataset below 50 pptv in the Arabian Sea, the Southern Red Sea, and the Eastern Mediterranean. In comparison, NO_x mixing ratios below 20 pptv were previously found e.g. over the South Atlantic (Fischer et al., 2015). The black lines in Fig. 1 represent two-day back trajectories (HYSPLIT, see Sect. 2.4). A similar figure for the 1st leg is given in Fig. S3. For the Mediterranean Sea, the Red Sea and the Arabian Gulf we present an analysis of the lifetimes and sources of NO_x and NO_z. Chemical sources of NO_x e.g. from the photolysis of HONO or pNit are discussed in Sect. 3.4. The chemically distinct regions are compared and contrasted in sections 3.5 and 4. Dividing the analysis into the three regions helps to highlight the chemically different environments encountered. An analysis of the Arabian Sea region was unfortunately not possible due to a gap in the NO_z measurements between 9 and 17 August 2017, caused by instrument failure during heavy seas and winds. The division into the regions was based on the prevalent NO_x mixing ratios displayed in Fig. S3c. In contrast to other AQABA publications (Eger et al., 2019a; Pfannerstill et al., 2019; Tadic et al., 2020), the Gulf of Oman and the Suez Channel were included in the Arabian Gulf and the Red Sea regions, respectively, as a clear shift in NO_x to mixing ratios below ca. 1 ppbv occurred both upon leaving the Gulf of Oman into the Arabian Sea and upon exiting the Suez Channel to the north towards the Mediterranean Sea. The transitions between the Arabian Gulf and the Gulf of Oman, and between the Northern Red Sea and the Suez region are less obviously represented in the NO_x levels.

3.1 Mediterranean Sea

Owing to unfavourable winds resulting in contamination of the measurements by the ships own exhaust as well as instrument malfunction, very little useable data was obtained by the TD-CRDS during the first leg through the Mediterranean Sea and we analyse only the data obtained on the return leg (24-31 August 2017). In this period, temperatures varied between 24 °C and 29 °C with relative humidity between 52 % and 89 % (see Fig S2). During most of the transit through the Mediterranean Sea, winds were from the north. At the end of the cruise when approaching Sicily we encountered a shift in wind direction with air arriving from the north-west. Back trajectories (see Fig. 1) indicate that when sailing through the Eastern Mediterranean Sea we encountered air masses that had passed over Turkey; the air we sampled in the central Mediterranean Sea had passed over the Balkan states and in the Western Mediterranean it had passed over Greece and Italy. The trajectories ending at the ships location were persistently located in the boundary layer (height < 1000 m) for the previous 48 hours. An exception was the back trajectory originating from the Black Sea, which was located at a height (above ground level) of up to 1740 m. The back trajectory passing over the island of Crete was located at a maximum height of 3224 m, which may be the result of orographic uplift caused by the central Cretan mountain range.

3.1.1 NO$_x$

NO$_x$ mixing ratios were generally low in the Mediterranean Sea (Fig. 2a)). One-minute mean and median mixing ratios of NO$_x$ as detected by the TD-CRDS were 1.3 and 0.3 ppbv, respectively. For the CLD measurements of NO$_x$, the equivalent values are 1.1 ppbv and 0.2 ppbv, respectively. For both instruments, the difference between mean and median values stems from the frequent occurrence of NO$_x$ plumes resulting from emissions of nearby ships. The NO$_x$ mixing ratios measured by TD-CRDS and CLD were in good agreement (see Friedrich et al. (2020)) and the bias of the TD-CRDS to higher values reflects the exclusion of data below the detection limit. A histogram of the NO$_x$ measurements made by the CLD is displayed in Fig. 2b) which indicates that 33 % of the NO$_x$ data were between 100 and 250 pptv, and 24 % above 1 ppbv. The maximum mixing ratio of NO$_x$ in the Mediterranean Sea of 84.7 ppbv was measured in the narrowest part of the Strait of Messina, a busy corridor for international shipping with ferry traffic between Italy and Sicily, crossing the *Kommandor Iona*'s ship track. This observation highlights the importance of NO$_x$ shipping emissions in some parts of the Mediterranean Sea, which we return to later.

Potential non-shipping sources of NO$_x$ in this region can be identified via the back trajectories plotted in Fig. 1: In the eastern part of the Mediterranean Sea, the air masses were influenced by emissions from the heavily populated and industrialized western Turkish coastal area, the island of Crete and mainland Greece. However, as we show below, the lifetime of NO$_x$ is generally less than 6 hours and the greater fraction of any land-based NO$_x$ emissions would have undergone oxidation to NO$_z$ during the 48 hour transport time of the back trajectory. In the Western Mediterranean Sea, the two-day back trajectories end above the open ocean.

Our data can be compared to results from previous measurements of NO$_x$ in the Mediterranean area. Excluding pollution events, Mallik et al. (2018) report NO and NO$_2$ levels below 0.05 ppbv and 0.25 ppbv, respectively, during the 2014 Cyprus-based CYPHEX campaign in the Eastern Mediterranean Sea. Plume-like increases in NO$_x$ were associated with enhanced SO$_2$ and related to emissions from shipping (Eger et al., 2019b). During the MINOS campaign on the island of Crete, median NO$_2$ mixing ratios between 0.3 ppbv and 0.7 ppbv were reported (Berresheim et al., 2003). The lower mixing ratios were associated with air masses arriving from the Western European free troposphere, whereas the higher values were air masses impacted by biomass burning in Eastern Europe. In contrast, higher NO$_2$ mixing ratios (typically between 4 ppbv and 6 ppbv excluding plumes) were reported from shipboard measurements in the Aegean Sea (Večeřa et al., 2008). Satellite based observations of NO$_2$ vertical column densities over Crete and in the region between Crete and Sicily, were used to derive near-surface NO$_2$ mixing ratios of up to ~ 0.4 ppbv (Ladstatter-Weissenmayer et al., 2003; Ladstatter-Weissenmayer et al., 2007).

Our NO$_x$ measurements are thus broadly consistent with previous measurements in the Mediterranean Sea which indicate mixing ratios of less than 1 ppbv in the absence of recent emissions from ships. The higher mixing ratios reported by Večeřa et al. (2008) are likely to be related to the close proximity of their ship to NO$_x$ sources on the European continent and denser ship traffic compared to the more southerly AQABA route through the Eastern Mediterranean Sea.

3.1.2 NO_z

260 Figures 2c) and d) show a time series and histogram of NO_z for the Mediterranean Sea. The shape of the distribution indicates that NO_z mixing ratios close to the detection limit were rarely measured. The mean (0.8 ppbv), median (0.7 ppbv), maximum (2.8 ppbv) and minimum NO_z mixing ratios (< 0.1 ppbv) along with the narrower distribution indicate that, as expected, NO_z is significantly less variable than NO_x. The ratio of the median mixing ratios NO_z / NO_y in the Mediterranean Sea is ~ 0.8; concomitantly, that of NO_x / NO_y is ~ 0.2. A more detailed analysis of the relative contributions of NO_x and NO_z to NO_y in

265 which we divide the Mediterranean Sea into 7 sub-regions, is presented in the following paragraphs. The choice of these sub-regions was based on the existence of homogeneous NO_z / NO_y ratios over periods of hours to days. This approach enabled us to compare sub-regions with substantially different chemical regimes along the ship track, but does not lend itself to the derivation of a representative NO_y budget for the entire region.

The pie charts in Fig. 3, indicate the regional average contributions (in sub-regions, M1 to M7) of reactive nitrogen species to

270 NO_y. The fractional contributions are based on measurements of NO_x, NO_y, gas-phase organic nitrates (ON), particulate nitrate (pNit), $ClNO_2$ and HONO. HNO_3 was not measured directly but calculated from $HNO_3 = NO_y – (NO_x + ON + pNit + ClNO_2 + HONO)$, where pNit refers to sub-micron particulate nitrate as measured by the HR-ToF-AMS. Detection of coarse mode pNit by the TD-CRDS (see Friedrich et al. (2020)) would lead to an overestimation of HNO_3. However, given that the thermal dissociation to NO_2 of $NaNO_3$ particles with 300 nm diameter is inefficient (~ 20 %) with this instrument, a significant bias

275 by coarse mode nitrate (e.g. associated with sea salt or mineral dust) appears unlikely. The data availaible in each sub-region did not always cover an entire diurnal cycle, which will have an impact on the fractional contributions of individual NO_y species (see differences between day- and nighttime chemistry in Sect. 1). We argue however, that diurnal patterns in NO_y are likely overshadowed by the variability of air mass sources. The NO_y compositions presented are thus to be considered as coarse estimates.

280 In all sub-regions, HNO_3 is the dominant component of NO_y besides NO_x and therefore the most important NO_z species. Contrastingly, sub-micron pNit only contributes between 5.4 % (M6) and 15.5 % (M2) to NO_y, and ONs between 7.1 % (M4) and 16.9 % (M2). $ClNO_2$ only constitutes a minor part of NO_y with ca. 1 % contribution in all regions where $ClNO_2$ was measured (M1-M6). The low mixing ratios of $ClNO_2$ have been attributed to high night-time temperatures and high reactivity of NO_3 which reduce the interaction of N_2O_5 with chloride containing particles (Eger et al., 2019a). Elevated HONO mixing

285 ratios (up to 0.3 ppbv) were observed in regions M3 and M6 where its contribution to NO_z was 3.8 % and 4.2 %, respectively. As the daytime lifetime of HONO is short (a few minutes) due to its rapid photolysis (Platt et al., 1980), HONO levels up to 0.3 ppbv imply strong sources. Elevated HONO mixing ratios in ship plumes have been observed in previous field measurements (Večeřa et al., 2008; Sun et al., 2020), and could explain the presence of HONO in sub-regions M3 and M6. Other sources of HONO, summarised in Elshorbany et al. (2012) include heterogeneous / photochemical reactions of NO_x and

290 NO_z on various surfaces and also the photolysis of particulate nitrate (Meusel et al., 2018).

Figure 3 also plots the NO_z / NO_y ratio along the ships track. The highest values with median $NO_z / NO_y > 0.68$ were found in regions M2, M4 and M7, reflecting a lack of local NO_x sources as confirmed by the back trajectories. For visual clarity, only the back trajectories starting at the geographical centres of the respective sub-regions are displayed in Fig. 3. Back trajectories starting at the ship's location 4 hours before or after confirmed that the air-mass origin was very similar. In contrast, the regions designated M3, M5 and M6 are influenced by fresh emissions from landbased sources and are characterised by low NO_z / NO_y ratios (medians < 0.55) reflecting the higher levels of NO_x which contributed 52 % (M3 and M5) and 43 % (M6) to total NO_y.

3.1.3 Lifetime and sources of NO_x

In the following section, the observations of NO_x in the Mediterranean Sea are analysed in terms of its production and loss. Following the considerations in Sect. 1, we compare the daytime loss of NO_x via the reaction between NO_2 and OH (R3; expected to dominate over other daytime NO_x loss processes in the marine environment) with night-time losses via the reaction between NO_2 and O_3 (R8):

$$k^{NO2} = k_3[OH] + k_8[O_3] \hspace{4cm} (1)$$

Where k^{NO2} represents the total loss rate constant (in s^{-1}) for NO_2 and is the inverse of the NO_2 lifetime (τ^{NO2}). The first term on the right-hand-side of this expression is most important at day when OH levels were high (up to 1.4×10^7 molecules cm^{-3} at local noon) but relatively unimportant at night. In contrast, the second term is only important at night as the NO_3 product of R8 is rapidly photolysed back to NO_x during daytime, so that NO_x is conserved.

By using Eq. 1 to approximate the NO_2 loss rate constant, we neglect two further processes which can, under some conditions, influence the lifetime of NO_2. Our approach assumes that the nighttime formation of NO_3 leads to the removal of one NO_2 molecule. This approach would be invalid, if a significant fraction of NO_3 would be lost via formation (and subsequent heterogeneous loss) of N_2O_5. Firstly, we note that formation of N_2O_5 was hindered during AQABA by the high gas-phase reactivity of NO_3 towards VOCs (Eger et al., 2019a) and that the transfer of N_2O_5 to the particle phase was hindered by high temperatures. For example, taking an N_2O_5 uptake coefficient γ_{N2O5} of 0.03 (as found for polluted marine environments by Aldener et al. (2006)) and the median nighttime aerosol surface area (ASA) in the Mediterranean Sea of 1.78×10^{-6} cm^2 cm^{-3} (Eger et al., 2019a), we estimated a loss rate constant for uptake of N_2O_5 of 3.5×10^{-4} s^{-1}, which is two orders of magnitude lower than the rate constant (4.9×10^{-2} s^{-1}) for thermal decomposition at 25.7 °C (the mean, minimum nighttime temperature in the Mediterranean Sea).

We also neglect the loss of NO_x via uptake of NO_2 onto black carbon (BC) particles. Using a literature uptake coefficient γ_{NO2} of ca. 1×10^{-4} (Longfellow et al., 1999) and the aforementioned ASA, the first order loss rate constant for the heterogeneous uptake would be 1.8×10^{-6} s^{-1}. Using an O_3 mixing ratio of 63.4 ppbv (= nighttime median mixing ratio in the Mediterranean Sea), we calculate a first-order loss rate constant for the reaction of NO_2 and O_3 of 5.5×10^{-5} s^{-1}, which implies that > 95 % of total NO_2 loss at nightime NO_2 is due to O_3. Uptake of NO_2 might therefore be relevant for HONO formation (see Sect. 3.4), but does not constitute a relevant loss process for NO_x.

In order to fill gaps in the OH dataset (daytime data coverage of 71 %) complete diel cycles of OH were generated by scaling measurements of J_{O1D} to the OH noon-time maxima. Figure S4 compares the measured OH concentrations with the interpolated trace and shows that the thereby derived OH levels can be considered as upper limits. Inserting these values and the measured O_3 concentration into Eq. 1 and using preferred rate coefficients for k_3 and k_8 (IUPAC, 2020) we derive lifetimes (Fig. 4a)) of ~ 2 hours at local noon (largest OH levels) and 5-6 hours at night. Loss of NO_x by deposition may be important in forested regions (Delaria et al., 2018; Delaria and Cohen, 2020) but is expected to be insignificant in a marine environment. The relative importance of day- and night-time losses of NO_2 in the Mediterranean Sea during AQABA was estimated by integrating the two loss terms using the available NO_2, O_3 and OH data. Averaged over the 6 days of measurements 3.71 ppbv of NO_x was lost per 12-hour day and 1.51 ppbv per 12-hour night (Fig. 4c)).

Although our conclusion is based on a limited dataset, we calculate that the OH-induced, daytime loss of NO_x is most important in the Mediterranean Sea, reflecting the high levels of OH encountered during AQABA, but note that night-time losses make a significant contribution. It is very likely that in other seasons with reduced photochemical activity and lower temperatures (which favour the formation of N_2O_5 which can remove two NO_2 molecules via heterogeneous processes), the night-time losses gain in relative importance. Averaged over the entire dataset obtained in the Mediterranean Sea, we calculate a lifetime of NO_2 of 3.9 hours. Chemical sources of NO_x in the Mediterranean Sea, i.e. from the photolysis of HONO and pNit, as well the reaction of OH and HNO_3, are discussed in detail in Sect. 3.4.

In the following, we examine the contribution of ship emissions to the NO_x budget in the Mediterranean region and especially along the track taken by the *Kommandor Iona* during the AQABA campaign. In Fig. S5 we plot a time series of NO_x and SO_2 data for the transit through the Mediterranean Sea. It is immediately apparent that large, plume like features in NO_x coincide with similar features in SO_2. We now separate the dataset into two regimes in which the NO_z and NO_y measurements indicate either relatively "fresh" emissions (NO_z / NO_y ratio < 0.4) or relatively "aged" emissions (NO_z / NO_y ratio > 0.8). In Fig. 5a) we show that, for fresh emissions, SO_2 and NO_x are highly correlated (Pearson's R = 0.84) with a slope of 4 ± 0.1 ppbv NO_x per ppbv SO_2 and an intercept (at zero SO_2) of -1.9 ± 0.3 ppbv. This strongly suggests that fresh NO_x emissions are generally accompanied by SO_2 and thus indicates that either ships or power plants, e.g. in coastal locations, are the likely sources of a large fraction of the NO_x. The slope is similar to that derived by Celik et al. (2020) (2.7 ± 0.8) who examined single ships plumes in a more detailed analysis and with literature values that range from 6.8 ± 6.3 near the coast of Texas (Williams et al., 2009) to 11.2 ± 10.9 (Diesch et al., 2013) at the Elbe river near Hamburg/Germany. In comparison to Celik et al. (2020), however, the two other literature studies only sampled very fresh and unprocessed ship plumes, from a distance of less than ca. 5 kilometres to the emission source. Fig. 5a) shows that NO_z and SO_2 are not correlated (Pearson's R = 0.38) in air masses impacted by fresh emissions.

In more aged air masses (Fig. 5b)) the slope of NO_x per SO_2 is, as expected, much smaller (0.16 ± 0.01 ppbv NO_2 per ppbv SO_2) which reflects the significantly longer lifetime of SO_2 (~ 10 days) compared to NO_x. After a few days of transport an air mass containing co-emitted NO_x and SO_2 will still contain SO_2 but the initially emitted NO_x will, to a large extent, have been

converted to NO_z. The intercept (NO_x = 0.049 ± 0.005 ppbv at zero SO_2) is consistent with the re-generation of NO_x from NO_z (see above), but is also in the area of the detection limit of the NO_x measurement.

The plot of NO_z versus SO_2 for aged emissions indicates a significant intercept (at zero SO_2) of 0.4 ppbv NO_z. As the lifetime of SO_2 (~ 10 days) is longer than of NO_z (~ half a day) (Dickerson et al., 1999; Romer et al., 2016) the residual NO_z at zero SO_2 cannot stem directly from ship emissions (or combustion sources that generate both NO_x and SO_2) but represents the background level of NO_z in the Mediterranean Sea in aged air masses and is consistent with an average HNO_3 mixing ratio of 0.48 ppbv observed during the MINOS campaign at Finokalia on Crete (Metzger et al., 2006).

The analysis above, when combined with back trajectory information, provides clear evidence that shipping emissions are responsible for a large fraction of NO_x in the Mediterranean Sea. The impact of shipping emissions on the atmospheric sulphur budget has been assessed in numerous studies which identify coastal areas and international shipping lanes as important hot spots for SO_2 emissions (Capaldo et al., 1999; Dalsoren et al., 2009; Eyring et al., 2010) with emissions of SO_2 severely impacting air quality in port-regions (Isakson et al., 2001; Cooper, 2003; Saxe and Larsen, 2004; Marmer and Langmann, 2005; Ledoux et al., 2018). A detailed analysis of SO_2 data with regard to ship emissions during AQABA is provided by Celik et al. (2020) who analysed emission factors from individual ships plumes during the AQABA campaign.

3.2 Red Sea

Measurements over the Red Sea (from the Suez Canal and the Strait of Bab al-Mandab) were made from 2-16 July 2017 on the first leg and 17-25 August 2017 on the second leg. On the first leg, the *Kommandor Iona* reversed direction in the Northern Red Sea three times (twice for nine hours and once for six hours), in order to sail into the wind and avoid contamination by the ship's own stack. Additionally, there was a three-day layover in Jeddah (10 to 13 July 2017). Temperatures on the first leg were usually above 27 °C, with maxima of 37-38 °C in the Suez Canal, in Jeddah and on the approach to Bab al-Mandab. The relative humidity was usually between ca. 60 % and 80 %, but dropped below 30 % in the Suez Canal and in Jeddah. Winds came predominantly from northerly directions with speeds generally between 2 and 10 m s⁻¹. On the second leg, temperatures were constantly above 30 °C in the Southern Red Sea, relative humidities were similar to the first leg. The wind was consistently from the north, with wind speeds between 5 and 12 m s⁻¹ until the ship reached the Suez region. During the first leg, the air masses intercepted above the Northern Red Sea were impacted by emissions from Cairo and the Nile valley. Two-day back trajectories for the Southern Red Sea start in the centre of the Red Sea and do not indicate transport from the Suez Region. Extended back trajectories for the Southern Red Sea showed that three to four days prior to sampling, the air parcel passed over southern Egypt, and five to six days before was located over the Cairo area. Similar back trajectories were obtained for the second leg. Air masses in the Northern Red Sea were influenced by the Suez region, north-eastern Egypt and Israel.

3.2.1 NO_x

NO_x mixing ratios in the Red Sea (excluding the three day layover in the port of Jeddah) as measured by the TD-CRDS and the CLD instruments are displayed in Fig. 6a). NO_x mixing ratios were highly variable and there were only short periods free

of NO_x plumes > 10 ppbv (e.g. during the second leg on 19 and 20 August 2017). The mean NO_x mixing ratios (2.8 ppbv measured by the TD-CRDS and 3.2 ppbv measured by the CLD) were therefore significantly higher than the median values of

390   1.0 ppbv. Figure 6b) indicates that the NO_x mixing ratios are broadly distributed around the median of 1.0 ppbv with 21 % of all data points > 3 ppbv. The highest NO_x levels during AQABA were found in narrow shipping corridors of the Suez region and the Strait of Bab al-Mandab. When excluding the Suez and Bab al-Mandab regions, a median NO_x mixing ratio of 0.7 ppbv can be derived for the maritime central part of the Red Sea.

To the best of our knowledge, in situ measurements in the Red Sea area are not available for comparison with our NO_x data.

395   Satellite based modelling studies show that high NO_2 column densities above the Red Sea are associated with shipping emissions (Richter et al., 2004; Alahmadi et al., 2019) which is consistent with our observation of a strong correlation between NO_x and SO_2 (see below). Johansson et al. (2017) have estimated a NO_x emission rate of 0.70 ton km^{-2} $yr^{-1}$for the Red Sea (including the Suez Region).

3.2.2 NO_z

400   The mean mixing ratio of NO_z over the Red Sea was 1.0 ppbv, with a maximum value of 8.0 ppbv measured in the Gulf of Suez on the first leg. NO_z mixing ratios are narrowly distributed (see Fig. 6d)) around a median value of 0.7 ppbv, with 53 % of the measurements between 0.4 and 1.0 ppbv, and 41 % between 1.0 and 4.0 ppbv.

The NO_z / NO_y ratios along the ships track are plotted in Fig. 7: values > 0.6 were mostly observed over the Northern Red Sea on the first leg, after leaving the Gulf of Suez. On the second leg, the NO_z / NO_y ratio was higher in the Southern Red Sea.

405   NO_z data coverage was limited in the Red Sea on both legs and the NO_z / NO_y ratio was more variable than values found in the Mediterranean Sea and the Arabian Gulf. The high variability in the NO_z / NO_y ratios is caused by the route of the *Kommandor Iona* along the main shipping lane connecting the Suez Canal and the Gulf of Aden and the frequent sampling of plumes from nearby ships. The observed NO_z / NO_y ratios of < 0.6 in the Red Sea highlight the impact of NO_x emissions from shipping on the reactive nitrogen budget and the air quality in the Red Sea region (as discussed in Sect. 3.2.1).

410   For the Red Sea, we have defined four sub-regions in which we calculate the contributions of NO_x and various NO_z species to NO_y: these are RS1 on the first leg and RS2, RS3 and RS4 on the second leg. Note that RS1 and RS4 are both located in the Northern Red Sea but the measurements (~5 weeks apart) revealed different chemical characteristics, hence the separate treatment.

Due to poor data coverage, mainly of organic nitrates, we were not able to perform this calculation in further sub-regions on

415   the first leg. In all four regions, NO_x was the largest component of NO_y which results from continuous NO_x input from on shore and shipping emissions.

In RS1 we observed the lowest contribution (36.4 %) of NO_x to NO_y and the largest contribution of ONs (23.8 %) to NO_y, over the Red Sea. The latter value is the highest found during the entire AQABA campaign and is comparable to the contribution of HNO_3 (30.0 %). In roughly co-located RS4, but 5 weeks later, the NO_x contribution was much larger (69.5 %).

420   The divergent median NO_x / NO_y and NO_z / NO_y for sub-regions RS1 and RS4 can be understood when one examines the air

mass back trajectories for the two legs. On the second leg, strong northerly winds transported NO_x from the highly polluted southern end of the Gulf of Suez to RS4, whereas during the first leg, the back trajectory for RS1 passed (with lower wind speeds) mainly over Eastern Egyptian deserts, with emissions from Cairo requiring 36 hours to reach RS1 during which a significant fraction of NO_x was converted to NO_z. We expect that the large contribution of ONs in RS1 is a result of the unique chemical environment at the southern end of the Gulf of Suez and in the Northern Red Sea. A large coherent oil field is located south of the Gulf of Suez and the coast of Eastern Egypt (Alsharhan, 2003) and the numerous facilities for oil extraction result in abundant emissions of VOCs while the proximity to the Gulf of Suez and the narrowing shipping corridor on the approach to Suez provides the NO_x required for formation of organic nitrates (ONs). Meteorological conditions additionally favored a buildup of ONs during our passage through RS1: elevated wind speeds of up to 11 m s^{-1} coincided with temperatures below 30 °C, which slowed down the thermal decomposition of PAN, compared to the ca. 35 °C regime in the Arabian Gulf. Average PAN mixing ratios, as measured by CIMS, were 190 pptv in this area, which constitutes ca. 20 % of the total ONs signal. On the second leg in RS4, the fractional contribution of ONs was overshadowed by the stronger impact of NO_x pollution from the Suez region (see above).

In RS1 and RS4 the contributions of HONO and $ClNO_2$ to NO_y were minor (≤ 3 %). RS2 and RS3 are both located in the southern half of the Red Sea. For RS3 we observed the highest contribution (15 %) of AMS-measured particulate nitrate to NO_y, and RS3 was characterised in large parts by coarse mode OPC fractions > 85 % (i.e. $(PM_{10}-PM_1)/PM_{10}$; see 18 and 19 August 2017 in Fig. S1). It is reasonable to assume that the coarse-mode particle mass concentrations in this area was due to sea salt, which reacts heterogeneously with HNO_3 to form particle-phase nitrates (Mamane and Gottlieb, 1990). Refractory sea salt aerosol particles in the PM_1 size range are, however, not expected to be detectable via AMS (Jimenez et al., 2003), or with only very low efficiency (ca. 1 %) (Zorn et al., 2008).

Region RS2 shows a intermediate behaviour, as NO_z / NO_y increases after leaving Bab al-Mandab and transported air only came from the surrounding Southern Red Sea without being influenced by shore side anthropogenic activities. Here, NO_x and HNO_3 contribute 57 % and 27 %, respectively. The relatively high NO_x contribution, considering the remote area, can be explained by sampling ships plumes on the departure from Bab el-Mandab, which led to several NO_x peaks above 10 ppbv (see Fig. 6a)). Consequently, background NO_x levels did also not fall below ca. 1.5 ppbv on the night from 17 to 18 August 2017. Overall, the fractional contributions of NO_x were positively biased by short term spikes in NO_x mixing ratios caused by ship plumes, in all Red Sea sub-regions. The use of mean values to assess the fractional contributions of NO_y species in certain sub-regions is thus a caveat of this analysis, as NO_z signals exhibit less variability during pollution events (see Fig. 6c)). Employing the median values, however, would not allow the relative contributions to NO_y to be assessed.

3.2.3 Lifetime and sources of NO_x

Analogous to Sect. 3.1.3, we now investigate the day- and night-time chemical losses of NO_2 in the Red Sea (see Fig. 8). As described previously, we used an interpolated OH data-set based on a scaling factor between the available OH data and J_{O1D}.

As OH was not measured over the Red Sea on the first leg, our analysis is restricted to the second leg only. Daytime NO_2 lifetimes w.r.t. loss by reaction with OH were usually in a range between 2 and 4 hours, with a minimum of 1.7 hours on 21 August 2017, where the noontime OH concentration peaked at 1.1×10^7 molecules cm^{-3}. Night-time NO_2 lifetimes (determined by O_3 levels) exhibited a larger variability, but were mostly between 5 and 10 hours. The average (day and night) NO_2 lifetime in the Red Sea was 5.0 hours.

Over the entire period of measurements in the Red Sea (8 days and 8 nights) we calculate that a cumulative total of 62 ppbv of NO_2 were lost (Fig 8c)). Despite the shorter lifetime of NO_2 at noon, the greater integrated loss of NO_2 occurred during nighttime (5.7 ppbv per night on average) when continually high O_3 levels (median 54 ppbv) were available. At midday, NO_2 mixing ratios are reduced due to the shift in the NO_2 / NO ratio caused by the rapid photolysis of NO_2 and also because the OH levels are highest then. On average, daytime loss rates were 2.0 ppbv per day.

In order to assess the contribution of shipping on NO_x emissions, we correlated NO_x and SO_2 mixing ratios for freshly emitted (NO_z / NO_y < 0.4) and chemically more aged (NO_z / NO_y > 0.8) air masses. The results are illustrated in Fig. 9 and summarized in Table 2, which reveal a positive correlation (slope of 3.7 ± 0.1 and a regression coefficient R of 0.61) between NO_x and SO_2 in air masses containing freshly emitted pollutants. Six data points far above 20 ppbv (range 43-128 ppbv SO_2) were excluded, as they would bias the linear regression result. Including these data points lowers the slope to 1.26 ± 0.04 and the correlation coefficient R to 0.40. The NO_x / SO_2 ratio is thus highly variable throughout the Red Sea, potentially reflecting variable NO_x / SO_2 emission ratios of different vessels, using various fuels, as well as the impact (on NO_x) of off offshore oil-drilling rigs and shore-side oil refineries. The latter are most important in the Northern Red Sea whereas shipping emissions dominate in the narrow shipping lanes of the Suez Canal.

For chemically aged air masses, the NO_x / SO_2 ratio is 0.20 ± 0.01 with R = 0.61, the reduction in slope reflecting the shorter lifetime of NO_x compared to SO_2. We find however, that in chemically aged air masses, NO_z and SO_2 are highly correlated (Fig. 9b)) with a slope NO_z / SO_2 = of 1.25 ± 0.04 and R = 0.85. The intercept (see Fig. 9b)) at an SO_2 mixing ratio of zero is $(0.40 \pm 0.03$ ppbv) which can be taken to be the regional NO_z background mixing ratio (i.e. NO_z formed from NO_x which was not emitted from SO_2-containing fuels).

3.3 Arabian Gulf

Data over the Arabian Gulf (see Fig. 10) were obtained from 24 to 31 July 2017 (first leg) and 31 July to 3 August 2017 (second leg). During the four-day layover in the harbour of Kuwait, the TD-CRDS was not operational. The highest temperatures during the AQABA campaign were found in the Arabian Gulf with daytime temperatures up to 46 °C at Kuwait harbour and 38-39 °C offshore. Nightime temperatures were constantly above 30 °C on both legs. Offshore relative humidities were between 60 and 90 % during both legs, wind speeds were generally below 6 m s^{-1}, and frequently 1-2 m s^{-1}. The Arabian Gulf crossing was divided into four sub-regions, A1 and A2 on the first, as well as A3 and A4 on the second leg (see Fig. 11). Air mass back trajectories indicated that air sampled in the Gulf of Oman originated in Oman, the south-eastern Arabian Gulf was influenced by transport from the central Arabian Gulf and Saudi-Arabia. Inside A1, samples were affected by the eastern

coast of Saudi Arabia. When approaching Kuwait (area A2), back trajectories pointed towards Iraq. During the second leg, the Northern Arabian Gulf region was dominated by stagnating air masses, mainly containing emissions from local sources and from the direction of Iran. Air from this area was also transported to the central Arabian Gulf, which is covered by sub-region A3. Local sources from inside the shipping lane were dominant when passing the Strait of Hormuz (A4). The Gulf of Oman experienced influx from the remote Arabian Sea, in contrast to the first leg.

3.3.1 NO$_x$

Elevated NO$_x$ mixing ratios were detected by both TD-CRDS and CLD throughout the Arabian Gulf (see Fig. 10a). The TD-CRDS measured mean and median NO$_x$ mixing ratios of 3.3 ppbv and 1.6 ppbv, respectively. By comparison, the CLD measured an average of 4.1 ppbv and a median of 1.8 ppbv. The large difference between median and mean reflects the numerous plumes of high NO$_x$ detected by both instruments (Fig. 10a), the deviation of the TD-CRDS and the CLD data is caused by different data coverage as the CLD continued measuring in the most polluted areas close to Fujairah and Kuwait, while the TD-CRDS was switched to zeroing mode, in order to avoid contamination of the inlet lines. When limiting the comparison to periods where both instruments were operating, very similar median values are obtained, with 1.6 ppbv from the TD-CRDS and 1.5 ppbv from the CLD, respectively. A histogram of the NO$_x$ measurements (CLD data only) made in the Arabian Gulf (Fig. 10b) shows a broad distribution, reflecting high variability in the region, with 77 % of the data points falling into a range between 0.4 ppbv and 10 ppbv and a broad maximum at 1-3 ppbv. The highest NO$_x$ daily maxima were observed near Fujairah (up to 34 ppbv on the first and 153 ppbv on the second leg), in the Strait of Hormuz (26 and 30 ppbv), and when approaching/departing Kuwait (43 and 90 ppbv). The locations of these maxima close to the shore or in narrow shipping corridors, and the plume-dominated time series suggest the influence of mostly local pollution sources of NO$_x$, i.e. from ship traffic or from industrial activities in the shore-side areas of the neighbouring cities. NO$_x$ mixing ratios < 0.5 ppbv were found exclusively in the central part of the Arabian Gulf, which is the widest part (least influence from on-shore activity) with the largest spread of the shipping lanes.

The generally very high levels of NO$_x$ in the Arabian Gulf are consistent with results from satellite measurements which have identified high NO$_2$ tropospheric vertical column densities over the Gulf of Oman, the Strait of Hormuz and the south-eastern Arabian Gulf (Beirle et al., 2004). Model studies estimate a NO$_x$ emission rate of 1.13 ton km^{-2} yr^{-1} for the Arabian Gulf (Johansson et al., 2017). With a NO$_x$ lifetime of 4.0 hours (see Sect. 3.3.3) and a boundary layer height of 1 km (Wu et al., 2008), this emission rate translates to a NO$_x$ mixing ratios of 0.3 ppbv. The lower mixing ratio, compared to the median NO$_x$ observed on AQABA (see above), is likely caused by the averaging of the model over the entire Arabian Gulf water surface area, whereas the *Kommandor Iona* followed common shipping routes with larger NO$_x$ emissions. To the best of our knowledge, there are no in-situ measurements of NO$_x$ over the Arabian Gulf, with which to compare our data.

3.3.2 NO_z

The Arabian Gulf featured the highest NO_z levels during the AQABA campaign (see Fig. 10c), with mixing ratios from < 0.1 ppbv up to 6.9 ppbv (mean 2.0 ± 1.5 ppbv (standard deviation), median 1.5 ± 0.7 ppbv (median absolute deviation)). The histogram of NO_z mixing ratios (Fig. 10d) shows a maximum in the frequency distribution at 1-3 ppbv, with 73 % of all data above 1 ppbv and 15 % above 4 ppbv. Our results thus indicate that the Arabian Gulf is a hotspot for NO_z formation, a result of high levels of the NO_x and VOCs precursors and also O_3. The spatial distribution of the NO_z / NO_y ratio for both legs is presented in Fig. 11. On both legs, NO_z / NO_y ratios above 0.8 were found in the central part of the Arabian Gulf, which results from the processing of NO_x emissions during transport from the shore to the centre of the Arabian Gulf.

We now examine the partitioning of NO_y into its various components in the four sub-regions (A1-A4) defined above for the Arabian Gulf (Fig. 11). On the approach to Kuwait (A2), winds from the north transported fresh NO_x emissions from cities in Kuwait and Iraq to the ship and NO_x accounted for 81 % of NO_y. More aged air masses were found in other regions (A1, A3, and A4) with a roughly equal split between NO_x and HNO_3 (both 45-50 %) observed in A3 and A4. The major component of NO_z was HNO_3 in all regions, with significant but very variable contribution from organic nitrates, especially in A1 (13 ± 16 %) where the air masses originated from the eastern coast of Saudi-Arabia, which accommodates numerous facilities for oil and gas extraction and processing resulting in high levels of organic trace gases including alkanes, alkenes and aromatics (Bourtsoukidis et al., 2019). Particulate nitrate contributed only minor amounts to NO_z in the Arabian Gulf which reflects the high temperatures and resultant partitioning of nitrate into the gas-phase. Other NO_z species contributed only weakly to the NO_z as indicated in Fig. 11.

3.3.3 Lifetime and sources of NO_x

Analogously to Sect. 3.1.3, we also determined NO_2 lifetimes and the cumulative loss of NO_2 in the Arabian Gulf. The results are presented in Fig. 12. Limited by the availability of OH data, these calculations include only the time period after 29 August 2017 on the first leg. In the same way as in Sect. 3.1.3 we used an interpolated OH data set in the following calculations.

In the Arabian Gulf, daytime NO_2 lifetimes (considering loss by OH) were generally between 2 and 4 hours. Night-time lifetimes were in a similar range, but also occasionally exceeded 10 hours, e.g. when leaving the Arabian Gulf towards the Gulf of Oman and the Arabian Sea on the second leg, where O_3 mixing ratios fell below 20 ppbv. The average NO_2 lifetime was calculated to be 4.0 hours.

Fig. 12c) shows that 50 ppbv NO_2 were lost cumulatively throughout the period of measurements over the Arabian Gulf, with night-time losses (black data points) being more important than daytime losses (red data points). On average 6.0 ppbv NO_2 were lost per night, and only 2.1 ppbv per day. Large night-time compared to day-time losses are related to moderate OH levels in large parts of the Arabian Gulf (see Fig. 12b)). The daytime average OH concentration was 2.4×10^6 molecules cm^{-3}, while on average 73 ppbv O_3 was present. The measured OH concentrations were generally low, given the NO_x and O_3 levels in the Arabian Gulf, which may have resulted from its reactions with VOCs. With a loss rate constant of 11.6 s^{-1}, the Arabian Gulf

was the AQABA region with the largest median OH reactivity (Pfannerstill et al., 2019), with 61 % of the total OH reactivity attributed to various measured VOCs. The daytime losses of NO_2 are therefore indirectly limited by the availability of VOCs from e.g. the oil and gas production (see above).

Via analysis of correlation between SO_2 and NO_2 (Fig. 13 and Table 2) we can assess the influence of shipping emissions on NO_x mixing ratios in the Arabian Gulf. In air masses recently influenced by NO_x emissions ($NO_z / NO_y < 0.4$), NO_x and SO_2 are only weakly correlated (slope = 4.1 ± 0.2, R = 0.41) indicating that many different NO_x sources (i.e. not only shipping emissions) contribute. These might include vehicular traffic and industrial activity (e.g. production of nitrogen-based fertilizers (Khan et al., 2016)) in Kuwait City, the Iraqi city of Basra, as well as in Iranian harbours and offshore oil and gas terminals. Considering the limited NO_x lifetime, the land-based emission sources of NO_x from urban/industrialised areas gain in importance over plumes from nearby ships, when approaching the coast. In aged air masses, the slope of the NO_x versus SO_2 correlation is 0.11 ± 0.01 with a large correlation coefficient (R = 0.72). This indicates that in aged air masses, the NO_x levels are linked to SO_2 emissions, which is consistent with the photolysis of HONO being a major source of NO_x in the region. From the intercept (SO_2 mixing ratio = zero = 0.0 ± 0.3 ppbv) we would expect negligible background levels of NO_z. Overall, shipping was an important source of NO_x in the Arabian Gulf, both through direct emissions and via photolysis of ship-related HONO.

3.4 NO_x and NO_y and the role of ship emission-related HONO formation during AQABA

In this section, we perform a steady-state analysis, assessing to what extent chemical source strengths can explain the background mixing ratios of NO_x observed during AQABA. Background conditions refer to NO_x mixing ratios found during periods when ship plumes were rarely encountered. "Background" NO_2 varied from region to region and was e.g. 50-150 pptv in the Mediterranean Sea). The required NO_x source strength (P, in molec cm^{-3} s^{-1}) to maintain the observed NO_x levels, is derived from the measured mixing ratios [NO_x], and the NO_2 reactivity (k^{NO2}; see Sect. 3.1.3), whereby $P = P_{chem} + E$ is a combination of chemical production (P_{chem}) and direct emission (E). Notably, we neglect direct emissions under background conditions (i.e. $E = 0$), and assume that NO_x is only lost via the reaction of NO_2 with OH (i.e. $k^{NOx} = k^{NO2}$).

$$P = [NO_x] \cdot k^{NO2} \tag{2}$$

Chemical processes that result in the formation of NO_x include the degradation of two gas-phase NO_z components, HONO and HNO_3 and the photolysis of particulate nitrate.

HONO + $h\nu$	$\rightarrow$	NO + OH	(R12)
OH + HNO_3	$\rightarrow$	NO_3 + H_2O	(R13)
pNit + $h\nu$	$\rightarrow$	2 HONO + 1 NO_x	(R14)

In a first step, we examine whether the HONO levels observed on AQABA can be explained by the photolysis of pNit in the PM_1 size range. This calculation is based on the assumption of a steady state for HONO established at noon through its photolytic loss, and its production through the photolysis of pNit. Using average noontime Mediterranean Sea concentrations

580   for HONO (2.44×10^9 molec cm^{-3}), and pNit (2.93×10^9 molec cm^{-3}), and a photolysis rate J_{HONO} (1.45×10^{-3} s^{-1}), we calculate that a value of J_{pNit} ~1.21×10^{-3} s^{-1} would be required in order to maintain the observed HONO concentrations. This is a factor ~ 5-6 higher than a reported value of J_{pNit} ~ 2×10^{-4} s^{-1}, based on observations over the western North Atlantic Ocean (Ye et al., 2016). It is however unclear whether the type and age of particles examined by (Ye et al., 2016) are comparable to those in AQABA. In addition, photolysable nitrate associated with particles that are > 1 μm diameter remain undetected by the AMS

585   and could also contribute to the discrepancy between required and literature J_{pNit}.

Laboratory studies have demonstrated the conversion of NO_2 to HONO on BC particles, with a clear enhancement under UV irradiation (Acker et al., 2006; Elshorbany et al., 2009; Monge et al., 2010; Ma et al., 2013). Monge et al. (2010) postulated the transport of HONO and NO to remote low-NO_x areas, enabled via this heterogeneous mechanism. Besides the effect of irradiation, heterogeneous, BC-assisted HONO and NO generation also shows a remarkable humidity dependence (Lammel

590   and Perner, 1988; Kalberer et al., 1999; Kleffmann et al., 1999). Further information on the particulate phase chemistry of HONO can be found in comprehensive reviews by Ma et al. (2013) and George et al. (2015). Sources of HONO during the AQABA campaign will be discussed in more detail, in a separate publication.

Using Eq. 2, we now calculate what values of P_{chem} are required to maintain the background levels of NO_x observed and assess the individual contributions from reactions R12-R14 (results presented in Table 3). The analysis was restricted to data points

595   where NO_z / NO_y was greater than 0.6 and to the four-hour timeframe around local noon, in order to focus on aged air mass conditions during maximum photochemical activity. NO_2 reacting with O_3 was not considered as a NO_x loss mechanism, due to the rapid reformation of NO_x by the photolysis of NO_3. For the pNit photolysis rate constant to form NO_x we used $0.33 \cdot J_{pNit}$ (from (Ye et al., 2016)), which accounts for the HONO / NO_x production ratio of 2:1. Additionally, we scaled J_{pNit} with J_{HONO} (normed to the average daytime maximum of J_{HONO}), to introduce diurnal variability. Due to limited data availability and rare

600   occurrence of $NO_z / NO_y > 0.6$ (i.e. sampling of aged air) in the other regions, we performed this calculation for the Mediterranean Sea only. The results indicate that the measured HONO concentrations should result in a factor ca. 4.7 times larger NO_x production term than calculated via Eq. 2. Possible explanations for this include a positively biased HONO measurement, or the underestimation of NO_x losses, e.g. due to undetected OH (despite the upper limit chosen in the interpolation). Our measurements and calculations, nonetheless, allow the qualitative identification of HONO photolysis as a

605   major source of daytime background NO_x levels during AQABA. The production rate from pNit photolysis can also account for ca. 64 % of the chemical NO_x generation, whereas the reaction of OH and HNO_3 forms an order of magnitude less NO_x.

Throughout AQABA, shipping emissions were responsible for fresh input of pollutant NO_x into the atmosphere. Our observation that levels of NO_x (with a lifetime of a few hours) were correlated with SO_2 (with lifetimes of more than a week) levels even in aged air masses and the observation that HONO photolysis was an important source of NO may be reconciled

610   by considering that HONO (and thus NO_x) production is driven by heterogeneous photochemistry on nitrate containing particulate matter, the formation of which is associated with emissions of NO_x and SO_2 as well as black carbon. The latter has a lifetime in the boundary layer (defined by its deposition) of about a week or longer in the absence of precipitation and is thus comparable to that of SO_2. The slow, photochemically induced conversion of nitrate to HONO thus provides a long-lived

source of NO_x and a link with SO_2, together with an explanation for the detection of short-lived HONO even in processed air masses in the Eastern Mediterranean Sea. We emphasise that the analysis presented here focussed on the daytime chemistry of HONO. At nighttime, a pseudo stationary state, independent of fresh NO_x input, has been observed by Wojtal et al. (2011), and explained with a reversible deposition of HONO on marine surfaces. This will however be insignificant during the day. Ship-derived HONO also has a substantial effect on the rates of photochemical O_3 formation in the remote marine boundary layer, largely as a result of higher RO_x production rates (Dai and Wang, 2021).

3.5 Inter-regional ozone production efficiency (OPE)

The OPE can be calculated from the relationship between O_x and NO_z where $O_x = O_3 + NO_2$ and the O_3 mixing ratios are augmented by those of NO_2, 95 % of which potentially photolyses to O_3 (Wood et al., 2009). Note that in any air mass where HNO_3 is a major component of NO_z, the derived OPE may represent an upper limit if HNO_3 is lost during transport from the NO_x source region to the measurement location. The NO_y / CO ratio has been used to estimate the impact of NO_z losses on the values of OPE obtained in this type of analysis (Nunnermacker et al., 2000) the rationale being that CO (like O_3) is a product of photochemical activity and relatively long lived, at least compared to NO_z. The high variability in the NO_y / CO ratio during AQABA is however indicative of local (non-photochemical) sources of CO e.g. via combustion and precludes use of this corrective procedure so that the values of OPE we present should be regarded as upper limits. An introduction into the OPE metric and on typical literature values is given in Sect. 1.

In Fig. 14 we plot O_x versus NO_z for which the NO_2 photolysis rate constant was $> 1 \times 10^{-3}$ s^{-1}, which restricts the analysis to hours of the day with active photochemistry. Regional OPE values are 10.5 ± 0.9 for the Red Sea, 19.1 ± 1.1 for the Arabian Gulf, and 15.4 ± 2.4 for the Eastern Mediterranean Sea. The heterogeneity of NO_z and O_3 mixing ratios, i.e. the chemical conditions frequently varying between aged and plume situations (see Sect. 3.1), resulted in a low correlation coefficient in the Western Mediterranean Sea ($R^2 = 0.19$), which precluded derivation of an OPE for this region and led us to restrict the Mediterranean Sea OPE analysis to the more homogenous eastern part (encompassing sub-regions M1-M5).

The range of OPE values measured during AQABA (10.5-19.1) is comparable to the value of 10, derived in the MBL at Oki Island, Japan, a site which is influenced by pollution arriving from the Korean peninsula and the Japanese mainland (Jaffe et al., 1996), but much lower than the value of 87 which was derived from observations off the coast of Newfoundland (Wang et al., 1996), where the median NO_x mixing ratio was < 100 pptv. As alluded to above, high values in remote locations may in part be a result of reactive nitrogen loss via deposition. By comparison, during AQABA the median NO_x mixing ratio was > 600 pptv, which together with the relatively low OPE indicates that the vast majority of the AQABA ship track cannot be considered representative of remote MBL conditions.

Figure 14 and Table 4 indicate that the Arabian Gulf, for which the highest O_3 levels in the entire campaign were found (up to 150 ppbv) also has the largest OPE, despite high median NO_x mixing ratios. The high OPE value, however, consistent with the analysis of Pfannerstill et al. (2019) who used VOC and OH reactivity measurements to derive the fraction of OH that reacts with VOCs (fuelling the formation of RO_2, conversion of NO to NO_2 and thus O_3 formation) versus the fraction that

reacted with NO_x (resulting in NO_z formation) to identify regions where O_3 formation was NO_x-limited, VOC-limited or (as was generally the case) in a transition regime. Pfannerstill et al. (2019) indicated that formation of O_3 was favoured around the Arabian Peninsula where VOCs from petroleum-extraction and processing industries were important sinks of OH. The highest net production rates of O_3 (NOPR) during AQABA were also found in the Arabian Gulf where calculations of the rate of RO_2 induced oxidation of NO to NO_2 resulted in a median (over the diel cycle) value of NOPR = 32 ppbv per day which was driven by high noon-time mixing ratios of RO_2 (73 pptv in the Arabian Gulf) (Tadic et al., 2020). In contrast to the OPE, NOPR accounts for the total amount of O_3 produced in one day, considering production (governed by the formation of NO_2 via reactions of NO with HO_2 and RO_2) and loss (via photolysis and reaction with OH or HO_2). The OPE, on the other hand, focusses on the product side and assesses the competition between O_3 formation and sequestering into NO_z from a given initial level of NO_x. By approximating the O_3 production rate via the NO_2 formation from NO reactions with HO_2 and RO_2, the NOPR thus neglects the alternative branch leading to NO_z. In the other two regions, the correlation coefficients are notably smaller, due to the lower span in O_3 and NO_z, resulting in increased relative errors for the derived OPE values.

In Fig. 15 we plot a time series of NO_z mixing ratios during the transition from the Arabian Sea to the Arabian Gulf along with NO_2 photolysis rates, O_3 and formaldehyde (HCHO) which is formed during the photochemical processing of many VOCs (Fischer et al., 2003; Klippel et al., 2011; Wolfe et al., 2016; Wolfe et al., 2019) and which can therefore be used as a tracer for photochemical activity (Dodge, 1990; Altshuller, 1993; Garcia et al., 2006; Duncan et al., 2010; Parrish et al., 2012). The transition from low NO_z levels in the Arabian Sea to values up to ~7 ppbv in the Strait of Hormuz (SH) is accompanied by increases in both O_3 (up to 160 ppbv) and HCHO (up to 12.5 ppbv). Based on the analysis by Duncan et al. (2010), Tadic et al. (2020) calculated a median HCHO / NO_2 ratio of 9.3 for the Arabian Gulf, indicating that O_3 production in this region is NO_x-limited. The high levels of NO_z, O_3 and HCHO in the Arabian Gulf result from the combination of intense solar radiation with high levels of reactive VOCs (Bourtsoukidis et al., 2019; Pfannerstill et al., 2019) and NO_x and are accompanied by the highest levels of gas-phase organic nitrates observed during AQABA, with absolute mixing ratios up to 2.5 ppbv on the approach to Kuwait. In conclusion, our NO_x/NO_y measurements and the OPE values derived from them confirm the exceptional photochemical activity in the Arabian Gulf.

4 Conclusions

During the AQABA campaign in the summer of 2017, we collected a unique NO_x and NO_y dataset that covers the Mediterranean Sea, the Red Sea, and the Arabian Gulf, regions with only few previously published observational data sets. The highest median NO_x and NO_z mixing ratios were observed in the Arabian Gulf (NO_x: 1.6 ppbv; NO_z: 1.5 ppbv), followed by the Red Sea (NO_x: 1.0 ppbv; NO_z: 0.7 ppbv) and the Mediterranean Sea (NO_x: 0.3 ppbv; NO_z: 0.7 ppbv). Night-time losses of NO_2 exceeded daytime losses by factors of 2.8 and 2.9 in the Arabian Gulf and the Red Sea, respectively, whereas daytime losses were 2.5 times higher in the Mediterranean Sea, a result of consistently high daytime OH-concentrations.

The derivation of NO_x lifetimes enabled us to calculate the NO_x source strength required to reproduce the observed mixing ratios and indicated that HONO photolysis was a significant source of NO_x in the Mediterranean Sea. The strong correlation between NO_x and SO_2 in air masses that were impacted by fresh emissions of NO_x indicated that ships are the dominant source of NO_x throughout the AQABA campaign. HONO may have been generated on particulate nitrate, possibly associated with black carbon that has been processed (to contain sulphate, organics and nitrate) as the ships plumes evolve chemically.

The fractional contributions to NO_x of NO_y and the various components of NO_z were highly variable in the three regions. The lowest regional mean contribution of NO_x to NO_y (i.e. most aged air masses) was found in the Mediterranean Sea with 41 % compared to 47 % in the Red Sea and 46 % in the Arabian Gulf. Of the NO_z trace-gases, HNO_3 represented the most important contribution to NO_y with 39 % in the Arabian Gulf, 25 % in the Red Sea and 35 % in the Mediterranean Sea. A clear regional variability was observed for the contribution of organic nitrates, with the highest value (16 % in the Red Sea) related to the concurrent availability of precursor NO_x and VOCs from the oil and gas industry. Comparable figures were derived for the Arabian Gulf and the Mediterranean Sea, with 10 % and 11 %, respectively. pNit (dp < 1 μm) contributed only a few percent, with the largest value (10 %) found in the Mediterranean Sea. HONO and $ClNO_2$ were generally only minor components (< 3 %) of NO_z. Future studies on the reactive nitrogen budget in the AQABA region might benefit from longer stationary measurements (e.g. to identify diurnal patterns), together with the detection of more speciated NO_z compounds (especially HNO_3 and ONs).

Data availability

All AQABA data sets used in this study are permanently stored in an archive on the KEEPER service of the Max Planck Digital Library (https://keeper.mpdl.mpg.de; last access: 4 December 2020), and are available to all scientists, which agree to the AQABA data protocol.

Author contributions

NF analysed the NO_x and NO_y data sets and wrote the manuscript. NF and JNC operated the TD-CRDS. PE and JNC provided CIMS measurements of SO_2 and $ClNO_2$. JSh, NS and JNC performed and evaluated ONs measurements. JSc set up and processed data from the spectral radiometer. DD, BH, IT and HF contributed NO, NO_2, HCHO and CO measurements. MM, RR, ST and HH provided OH concentrations. EYP, NW and JW were responsible for the OH reactivity measurements. JB and FD performed measurements with the AMS and OPC instruments. HS, GL and YC contributed the HONO data set. JL designed the AQABA campaign. All authors contributed to the writing of the manuscript.

Competing interests

The authors declare that they have no conflict of interest.

Acknowledgements

The authors gratefully acknowledge the NOAA Air Resources Laboratory (ARL) for the provision of the HYSPLIT transport and dispersion model and READY website (https://www.ready.noaa.gov) used in this publication. We thank the whole crew of the *Kommandor Iona* and Hays Ships for their support, as well as Marcel Dorf for organising the campaign.

References

Acker, K., Febo, A., Trick, S., Perrino, C., Bruno, P., Wiesen, P., Moller, D., Wieprecht, W., Auel, R., Giusto, M., Geyer, A., Platt, U., and Allegrini, I.: Nitrous acid in the urban area of Rome, Atmos Environ, 40, 3123-3133, 10.1016/j.atmosenv.2006.01.028, 2006.

Alahmadi, S., Al-Ahmadi, K., and Almeshari, M.: Spatial variation in the association between NO2 concentrations and shipping emissions in the Red Sea, Science of the Total Environment, 676, 131-143, 10.1016/j.scitotenv.2019.04.161, 2019.

Aldener, M., Brown, S. S., Stark, H., Williams, E. J., Lerner, B. M., Kuster, W. C., Goldan, P. D., Quinn, P. K., Bates, T. S., Fehsenfeld, F. C., and Ravishankara, A. R.: Reactivity and loss mechanisms of NO_3 and N_2O_5 in a polluted marine environment: Results from in situ measurements during New England Air Quality Study 2002, Journal of Geophysical Research-Atmospheres, 111, art. D23S73, doi 10.1029/2006JD007252, 2006.

Alsharhan, A. S.: Petroleum geology and potential hydrocarbon plays in the Gulf of Suez rift basin, Egypt, Aapg Bull, 87, 143-180, 2003.

Altshuller, A. P.: Production of Aldehydes as Primary Emissions and from Secondary Atmospheric Reactions of Alkenes and Alkanes during the Night and Early Morning Hours, Atmospheric Environment Part a-General Topics, 27, 21-32, Doi 10.1016/0960-1686(93)90067-9, 1993.

Beirle, S., Platt, U., von Glasow, R., Wenig, M., and Wagner, T.: Estimate of nitrogen oxide emissions from shipping by satellite remote sensing, Geophysical Research Letters, 31, Artn L18102
10.1029/2004gl020312, 2004.

Berresheim, H., Plass-Dulmer, C., Elste, T., Mihalopoulos, N., and Rohrer, F.: OH in the coastal boundary layer of Crete during MINOS: Measurements and relationship with ozone photolysis, Atmospheric Chemistry and Physics, 3, 639-649, DOI 10.5194/acp-3-639-2003, 2003.

Bohn, B., Corlett, G. K., Gillmann, M., Sanghavi, S., Stange, G., Tensing, E., Vrekoussis, M., Bloss, W. J., Clapp, L. J., Kortner, M., Dorn, H. P., Monks, P. S., Platt, U., Plass-Dulmer, C., Mihalopoulos, N., Heard, D. E., Clemitshaw, K. C., Meixner, F. X., Prevot, A. S. H., and Schmitt, R.: Photolysis frequency measurement techniques: results of a comparison within the ACCENT project, Atmospheric Chemistry and Physics, 8, 5373-5391, 2008.

Bourtsoukidis, E., Ernle, L., Crowley, J. N., Lelieveld, J., Paris, J. D., Pozzer, A., Walter, D., and Williams, J.: Non-methane hydrocarbon (C-2-C-8) sources and sinks around the Arabian Peninsula, Atmospheric Chemistry and Physics, 19, 7209-7232, 10.5194/acp-19-7209-2019, 2019.

Bourtsoukidis, E., Pozzer, A., Sattler, T., Matthaios, V. N., Ernle, L., Edtbauer, A., Fischer, H., Könemann, T., Osipov, S., Paris, J. D., Pfannerstill, E. Y., Stönner, C., Tadic, I., Walter, D., Wang, N., Lelieveld, J., and Williams, J.: The Red Sea Deep Water is a potent source of atmospheric ethane and propane, Nature Communications, 11, 447, 10.1038/s41467-020-14375-0, 2020.

Burkholder, J. B., Sander, S. P., Abbatt, J., Barker, J. R., Huie, R. E., Kolb, C. E., Kurylo, M. J., Orkin, V. L., Wilmouth, D. M., and Wine, P. H.: Chemical Kinetics and Photochemical Data for Use in Atmospheric Studies, Evaluation No. 18," JPL Publication 15-10, Jet Propulsion Laboratory, Pasadena, http://jpldataeval.jpl.nasa.gov., 2015.

Capaldo, K., Corbett, J. J., Kasibhatla, P., Fischbeck, P., and Pandis, S. N.: Effects of ship emissions on sulphur cycling and radiative climate forcing over the ocean, Nature, 400, 743-746, Doi 10.1038/23438, 1999.

Celik, S., Drewnick, F., Fachinger, F., Brooks, J., Darbyshire, E., Coe, H., Paris, J. D., Eger, P. G., Schuladen, J., Tadic, I., Friedrich, N., Dienhart, D., Hottmann, B., Fischer, H., Crowley, J. N., Harder, H., and Borrmann, S.: Influence of vessel characteristics and atmospheric processes on the gas and particle phase of ship emission plumes: in situ measurements in the Mediterranean Sea and around the Arabian Peninsula, Atmos Chem Phys, 20, 4713-4734, 10.5194/acp-20-4713-2020, 2020.

Chameides, W. L., Stedman, D. H., Dickerson, R. R., Rusch, D. W., and Cicerone, R. J.: Nox Production in Lightning, Journal of the Atmospheric Sciences, 34, 143-149, Doi 10.1175/1520-0469(1977)034<0143:Npil>2.0.Co;2, 1977.

Cooper, D. A.: Exhaust emissions from ships at berth, Atmospheric Environment, 37, 3817-3830, 10.1016/S1352-2310(03)00446-1, 2003.

Dai, J., and Wang, T.: Impact of International Shipping Emissions on Ozone and PM2.5: The Important Role of HONO and ClNO2, Atmos. Chem. Phys. Discuss., 2021, 1-29, 10.5194/acp-2020-1185, 2021.

770

Dalsoren, S. B., Eide, M. S., Endresen, O., Mjelde, A., Gravir, G., and Isaksen, I. S. A.: Update on emissions and environmental impacts from the international fleet of ships: the contribution from major ship types and ports, Atmospheric Chemistry and Physics, 9, 2171-2194, DOI 10.5194/acp-9-2171-2009, 2009.

775 Daum, P. H., Kleinman, L., Imre, D. G., Nunnermacker, L. J., Lee, Y. N., Springston, S. R., Newman, L., and Weinstein-Lloyd, J.: Analysis of the processing of Nashville urban emissions on July 3 and July 18, 1995, J Geophys Res-Atmos, 105, 9155-9164, Doi 10.1029/1999jd900997, 2000.

Davis, D. D., Crawford, J., Chen, G., Chameides, W., Liu, S., Bradshaw, J., Sandholm, S., Sachse, G., Gregory, G., Anderson, B., Barrick, 780 J., Bachmeier, A., Collins, J., Browell, E., Blake, D., Rowland, S., Kondo, Y., Singh, H., Talbot, R., Heikes, B., Merrill, J., Rodriguez, J., and Newell, R. E.: Assessment of ozone photochemistry in the western North Pacific as inferred from PEM-West A observations during the fall 1991, J Geophys Res-Atmos, 101, 2111-2134, Doi 10.1029/95jd02755, 1996.

Day, D. A., Dillon, M. B., Wooldridge, P. J., Thornton, J. A., Rosen, R. S., Wood, E. C., and Cohen, R. C.: On alkyl nitrates, O$_3$, and the 785 "missing NOy", Journal of Geophysical Research-Atmospheres, 108, 4501, doi:10.1029/2003jd003685, 2003.

DeCarlo, P. F., Kimmel, J. R., Trimborn, A., Northway, M. J., Jayne, J. T., Aiken, A. C., Gonin, M., Fuhrer, K., Horvath, T., Docherty, K. S., Worsnop, D. R., and Jimenez, J. L.: Field-deployable, high-resolution, time-of-flight aerosol mass spectrometer, Analytical Chemistry, 78, 8281-8289, 10.1021/ac061249n, 2006.

790

Delaria, E. R., Vieira, M., Cremieux, J., and Cohen, R. C.: Measurements of NO and NO$_2$ exchange between the atmosphere and Quercus agrifolia, Atmos Chem Phys, 18, 14161-14173, 10.5194/acp-18-14161-2018, 2018.

Delaria, E. R., and Cohen, R. C.: A model-based analysis of foliar NOx deposition, Atmos. Chem. Phys., 20, 2123-2141, 10.5194/acp-20-795 2123-2020, 2020.

Dickerson, R. R., Rhoads, K. P., Carsey, T. P., Oltmans, S. J., Burrows, J. P., and Crutzen, P. J.: Ozone in the remote marine boundary layer: A possible role for halogens, Journal of Geophysical Research-Atmospheres, 104, 21385-21395, 1999.

800 Diesch, J. M., Drewnick, F., Klimach, T., and Borrmann, S.: Investigation of gaseous and particulate emissions from various marine vessel types measured on the banks of the Elbe in Northern Germany, Atmospheric Chemistry and Physics, 13, 3603-3618, 10.5194/acp-13-3603-2013, 2013.

Dodge, M. C.: Formaldehyde Production in Photochemical Smog as Predicted by 3 State-of-the-Science Chemical Oxidant Mechanisms, 805 Journal of Geophysical Research-Atmospheres, 95, 3635-3648, DOI 10.1029/JD095iD04p03635, 1990.

Duncan, B. N., Yoshida, Y., Olson, J. R., Sillman, S., Martin, R. V., Lamsal, L., Hu, Y. T., Pickering, K. E., Retscher, C., Allen, D. J., and Crawford, J. H.: Application of OMI observations to a space-based indicator of NOx and VOC controls on surface ozone formation, Atmospheric Environment, 44, 2213-2223, 10.1016/j.atmosenv.2010.03.010, 2010.

810

Edtbauer, A., Stönner, C., Pfannerstill, E. Y., Berasategui, M., Walter, D., Crowley, J. N., Lelieveld, J., and Williams, J.: A new marine biogenic emission: methane sulfonamide (MSAM), dimethyl sulfide (DMS), and dimethyl sulfone (DMSO2) measured in air over the Arabian Sea, Atmos. Chem. Phys., 20, 6081-6094, 10.5194/acp-20-6081-2020, 2020.

815 Eger, P. G., Friedrich, N., Schuladen, J., Shenolikar, J., Fischer, H., Tadic, I., Harder, H., Martinez, M., Rohloff, R., Tauer, S., Drewnick, F., Fachinger, F., Brooks, J., Darbyshire, E., Sciare, J., Pikridas, M., Lelieveld, J., and Crowley, J. N.: Shipborne measurements of ClNO2 in the Mediterranean Sea and around the Arabian Peninsula during summer, Atmospheric Chemistry and Physics, 19, 12121-12140, 10.5194/acp-19-12121-2019, 2019a.

820 Eger, P. G., Helleis, F., Schuster, G., Phillips, G. J., Lelieveld, J., and Crowley, J. N.: Chemical ionization quadrupole mass spectrometer with an electrical discharge ion source for atmospheric trace gas measurement, Atmos. Meas. Tech., 12, 1935-1954, 10.5194/amt-12-1935-2019, 2019b.

Elshorbany, Y. F., Kurtenbach, R., Wiesen, P., Lissi, E., Rubio, M., Villena, G., Gramsch, E., Rickard, A. R., Pilling, M. J., and Kleffmann, J.: Oxidation capacity of the city air of Santiago, Chile, Atmos Chem Phys, 9, 2257-2273, DOI 10.5194/acp-9-2257-2009, 2009.

Elshorbany, Y. F., Steil, B., Brühl, C., and Lelieveld, J.: Impact of HONO on global atmospheric chemistry calculated with an empirical parameterization in the EMAC model, Atmos. Chem. Phys., 12, 9977-10000, 10.5194/acp-12-9977-2012, 2012.

Eyring, V., Isaksen, I. S. A., Berntsen, T., Collins, W. J., Corbett, J. J., Endresen, O., Grainger, R. G., Moldanova, J., Schlager, H., and Stevenson, D. S.: Transport impacts on atmosphere and climate: Shipping, Atmospheric Environment, 44, 4735-4771, 10.1016/j.atmosenv.2009.04.059, 2010.

Fischer, H., Kormann, R., Klupfel, T., Gurk, C., Konigstedt, R. K., Parchatka, U., Muhle, J., Rhee, T. S., Brenninkmeijer, C. A. M., Bonasoni, P., and Stohl, A.: Ozone production and trace gas correlations during the June 2000 MINATROC intensive measurement campaign at Mt. Cimone, Atmospheric Chemistry and Physics, 3, 725-738, 10.5194/acp-3-725-2003, 2003.

Fischer, H., Pozzer, A., Schmitt, T., Jockel, P., Klippel, T., Taraborrelli, D., and Lelieveld, J.: Hydrogen peroxide in the marine boundary layer over the South Atlantic during the OOMPH cruise in March 2007, Atmospheric Chemistry and Physics, 15, 6971-6980, 2015.

Fried, A., McKeen, S., Sewell, S., Harder, J., Henry, B., Goldan, P., Kuster, W., Williams, E., Baumann, K., Shetter, R., and Cantrell, C.: Photochemistry of formaldehyde during the 1993 Tropospheric OH Photochemistry Experiment, Journal of Geophysical Research-Atmospheres, 102, 6283-6296, Doi 10.1029/96jd03249, 1997.

Friedrich, N., Tadic, I., Schuladen, J., Brooks, J., Darbyshire, E., Drewnick, F., Fischer, H., Lelieveld, J., and Crowley, J. N.: Measurement of NOx and NOy with a thermal dissociation cavity ring-down spectrometer (TD-CRDS): instrument characterisation and first deployment, Atmos Meas Tech, 13, 5739-5761, 10.5194/amt-13-5739-2020, 2020.

Garcia, A. R., Volkamer, R., Molina, L. T., Molina, M. J., Samuelson, J., Mellqvist, J., Galle, B., Herndon, S. C., and Kolb, C. E.: Separation of emitted and photochemical formaldehyde in Mexico City using a statistical analysis and a new pair of gas-phase tracers, Atmospheric Chemistry and Physics, 6, 4545-4557, DOI 10.5194/acp-6-4545-2006, 2006.

Ge, B. Z., Sun, Y. L., Liu, Y., Dong, H. B., Ji, D. S., Jiang, Q., Li, J., and Wang, Z. F.: Nitrogen dioxide measurement by cavity attenuated phase shift spectroscopy (CAPS) and implications in ozone production efficiency and nitrate formation in Beijing, China, J Geophys Res-Atmos, 118, 9499-9509, 10.1002/jgrd.50757, 2013.

George, C., Ammann, M., D'Anna, B., Donaldson, D. J., and Nizkorodov, S. A.: Heterogeneous Photochemistry in the Atmosphere, Chem Rev, 115, 4218-4258, 10.1021/cr500648z, 2015.

Heland, J., Kleffmann, J., Kurtenbach, R., and Wiesen, P.: A new instrument to measure gaseous nitrous acid (HONO) in the atmosphere, Environmental Science & Technology, 35, 3207-3212, DOI 10.1021/es000303t, 2001.

Isakson, J., Persson, T. A., and Lindgren, E. S.: Identification and assessment of ship emissions and their effects in the harbour of G(o)over-circleteborg, Sweden, Atmospheric Environment, 35, 3659-3666, Doi 10.1016/S1352-2310(00)00528-8, 2001.

IUPAC: Task Group on Atmospheric Chemical Kinetic Data Evaluation, (Ammann, M., Cox, R.A., Crowley, J.N., Herrmann, H., Jenkin, M.E., McNeill, V.F., Mellouki, A., Rossi, M. J., Troe, J. and Wallington, T. J.) http://iupac.pole-ether.fr/index.html., 2020.

Jaffe, D. A., Honrath, R. E., Zhang, L., Akimoto, H., Shimizu, A., Mukai, H., Murano, K., Hatakeyama, S., and Merrill, J.: Measurements of NO, NOy, CO and O3 and estimation of the ozone production rate at Oki Island, Japan, during PEM-West, J Geophys Res-Atmos, 101, 2037-2048, Doi 10.1029/95jd01699, 1996.

Jimenez, J. L., Jayne, J. T., Shi, Q., Kolb, C. E., Worsnop, D. R., Yourshaw, I., Seinfeld, J. H., Flagan, R. C., Zhang, X. F., Smith, K. A., Morris, J. W., and Davidovits, P.: Ambient aerosol sampling using the Aerodyne Aerosol Mass Spectrometer, Journal of Geophysical Research-Atmospheres, 108, 10.1029/2001jd001213, 2003.

Johansson, L., Jalkanen, J. P., and Kukkonen, J.: Global assessment of shipping emissions in 2015 on a high spatial and temporal resolution, Atmospheric Environment, 167, 403-415, 10.1016/j.atmosenv.2017.08.042, 2017.

880 Kalberer, M., Ammann, M., Arens, F., Gaggeler, H. W., and Baltensperger, U.: Heterogeneous formation of nitrous acid (HONO) on soot aerosol particles, Journal of Geophysical Research-Atmospheres, 104, 13825-13832, 1999.

Kercher, J. P., Riedel, T. P., and Thornton, J. A.: Chlorine activation by N2O5: simultaneous, in situ detection of ClNO2 and N2O5 by chemical ionization mass spectrometry, Atmospheric measurement techniques, 2, 193-204, 2009.
885
Khan, A. R., Al-Awadi, L., and Al-Rashidi, M. S.: Control of ammonia and urea emissions from urea manufacturing facilities of Petrochemical Industries Company (PIC), Kuwait, Journal of the Air & Waste Management Association, 66, 609-618, 10.1080/10962247.2016.1145154, 2016.

890 Kleffmann, J., Becker, K. H., Lackhoff, M., and Wiesen, P.: Heterogeneous conversion of NO2 on carbonaceous surfaces, Physical Chemistry Chemical Physics, 1, 5443-5450, DOI 10.1039/a905545b, 1999.

Klippel, T., Fischer, H., Bozem, H., Lawrence, M. G., Butler, T., Jockel, P., Tost, H., Martinez, M., Harder, H., Regelin, E., Sander, R., Schiller, C. L., Stickler, A., and Lelieveld, J.: Distribution of hydrogen peroxide and formaldehyde over Central Europe during the HOOVER
895 project, Atmospheric Chemistry and Physics, 11, 4391-4410, 10.5194/acp-11-4391-2011, 2011.

Ladstatter-Weissenmayer, A., Heland, J., Kormann, R., von Kuhlmann, R., Lawrence, M. G., Meyer-Arnek, J., Richter, A., Wittrock, F., Ziereis, H., and Burrows, J. P.: Transport and build-up of tropospheric trace gases during the MINOS campaign: comparision of GOME, in situ aircraft measurements and MATCH-MPIC-data, Atmospheric Chemistry and Physics, 3, 1887-1902, DOI 10.5194/acp-3-1887-2003,
900 2003.

Ladstatter-Weissenmayer, A., Kanakidou, M., Meyer-Arnek, J., Dermitzaki, E. V., Richter, A., Vrekoussis, M., Wittrock, F., and Burrows, J. P.: Pollution events over the East Mediterranean: Synergistic use of GOME, ground-based and sonde observations and models, Atmospheric Environment, 41, 7262-7273, 10.1016/j.atmosenv.2007.05.031, 2007.
905
Lammel, G., and Perner, D.: The Atmospheric Aerosol as a Source of Nitrous-Acid in the Polluted Atmosphere, Journal of Aerosol Science, 19, 1199-1202, Doi 10.1016/0021-8502(88)90135-8, 1988.

Lange, L., Hoor, P., Helas, G., Fischer, H., Brunner, D., Scheeren, B., Williams, J., Wong, S., Wohlfrorn, K. H., Arnold, F., Strom, J., Krejci,
910 R., Lelieveld, J., and Andreae, M. O.: Detection of lightning-produced NO in the midlatitude upper troposphere during STREAM 1998, Journal of Geophysical Research-Atmospheres, 106, 27777-27785, Doi 10.1029/2001jd900210, 2001.

Ledoux, F., Roche, C., Cazier, F., Beaugard, C., and Courcot, D.: Influence of ship emissions on NOx, SO2, O3 and PM concentrations in a North-Sea harbor in France, J Environ Sci-China, 71, 56-66, 10.1016/j.jes.2018.03.030, 2018.
915
Lelieveld, J., Hoor, P., Jöckel, P., Pozzer, A., Hadjinicolaou, P., Cammas, J.-P., and Beirle, S.: Severe ozone air pollution in the Persian Gulf region, Atmospheric Chemistry and Physics, 9, 10.5194/acp-9-1393-2009, 2009.

Lelieveld, J., Hadjinicolaou, P., Kostopoulou, E., Chenoweth, J., El Maayar, M., Giannakopoulos, C., Hannides, C., Lange, M. A., Tanarhte,
920 M., Tyrlis, E., and Xoplaki, E.: Climate change and impacts in the Eastern Mediterranean and the Middle East, Climatic Change, 114, 667-687, 10.1007/s10584-012-0418-4, 2012.

Lenner, M.: Nitrogen-Dioxide in Exhaust Emissions from Motor-Vehicles, Atmospheric Environment, 21, 37-43, Doi 10.1016/0004-6981(87)90268-X, 1987.
925
Lewis, E. R., and Schwartz, S. E.: Sea salt aerosol production : mechanisms, methods, measurements and models : a critical review, Geophysical monograph, 152, American Geophysical Union, Washington, DC, xii, 413 p. pp., 2004.

Li, J. S., Parchatka, U., and Fischer, H.: Development of field-deployable QCL sensor for simultaneous detection of ambient N2O and CO,
930 Sensor Actuat B-Chem, 182, 659-667, 10.1016/j.snb.2013.03.073, 2013.

Lin, W., Xu, X., Ge, B., and Liu, X.: Gaseous pollutants in Beijing urban area during the heating period 2007-2008: variability, sources, meteorological, and chemical impacts, Atmos Chem Phys, 11, 8157-8170, 10.5194/acp-11-8157-2011, 2011.

935   Liu, S. C., Trainer, M., Fehsenfeld, F. C., Parrish, D. D., Williams, E. J., Fahey, D. W., Hubler, G., and Murphy, P. C.: Ozone Production in the Rural Troposphere and the Implications for Regional and Global Ozone Distributions, Journal of Geophysical Research-Atmospheres, 92, 4191-4207, DOI 10.1029/JD092iD04p04191, 1987.

Logan, J. A.: Nitrogen-Oxides in the Troposphere - Global and Regional Budgets, Journal of Geophysical Research-Oceans, 88, 785-807,
940   DOI 10.1029/JC088iC15p10785, 1983.

Longfellow, C. A., Ravishankara, A. R., and Hanson, D. R.: Reactive uptake on hydrocarbon soot: Focus on NO2, Journal of Geophysical Research-Atmospheres, 104, 13833-13840, 1999.

945   Ma, J. Z., Liu, Y. C., Han, C., Ma, Q. X., Liu, C., and He, H.: Review of heterogeneous photochemical reactions of NOy on aerosol - A possible daytime source of nitrous acid (HONO) in the atmosphere, J Environ Sci, 25, 326-334, 10.1016/S1001-0742(12)60093-X, 2013.

Mallik, C., Tomsche, L., Bourtsoukidis, E., Crowley, J. N., Derstroff, B., Fischer, H., Hafermann, S., Hüser, I., Javed, U., Keßel, S., Lelieveld, J., Martinez, M., Meusel, H., Novelli, A., Phillips, G. J., Pozzer, A., Reiffs, A., Sander, R., Taraborrelli, D., Sauvage, C.,
950   Schuladen, J., Su, H., Williams, J., and Harder, H.: Oxidation processes in the eastern Mediterranean atmosphere: evidence from the modelling of HOx measurements over Cyprus, Atmospheric Chemistry and Physics, 18, 10825-10847, 10.5194/acp-18-10825-2018, 2018.

Mamane, Y., and Gottlieb, J.: Heterogeneous reaction of nitrogen oxides on sea salt and mineral particles- A single particle approach, JAS, 21, 225-228, 1990.
955

Marmer, E., and Langmann, B.: Impact of ship emissions on the Mediterranean summertime pollution and climate: A regional model study, Atmospheric Environment, 39, 4659-4669, 10.1016/j.atmosenv.2005.04.014, 2005.

Martinez, M., Harder, H., Kubistin, D., Rudolf, M., Bozem, H., Eerdekens, G., Fischer, H., Kluepfel, T., Gurk, C., Koenigstedt, R., Parchatka,
960   U., Schiller, C. L., Stickler, A., Williams, J., and Lelieveld, J.: Hydroxyl radicals in the tropical troposphere over the Suriname rainforest: airborne measurements, Atmospheric Chemistry and Physics, 10, 3759-3773, 2010.

Metzger, S., Mihalopoulos, N., and Lelieveld, J.: Importance of mineral cations and organics in gas-aerosol partitioning of reactive nitrogen compounds: case study based on MINOS results, Atmospheric Chemistry and Physics, 6, 2549-2567, DOI 10.5194/acp-6-2549-2006, 2006.
965

Meusel, H., Tamm, A., Kuhn, U., Wu, D. M., Leifke, A. L., Fiedler, S., Ruckteschler, N., Yordanova, P., Lang-Yona, N., Pohlker, M., Lelieveld, J., Hoffmann, T., Poschl, U., Su, H., Weber, B., and Cheng, Y. F.: Emission of nitrous acid from soil and biological soil crusts represents an important source of HONO in the remote atmosphere in Cyprus, Atmos Chem Phys, 18, 799-813, 10.5194/acp-18-799-2018, 2018.
970

Monge, M. E., D'Anna, B., Mazri, L., Giroir-Fendler, A., Ammann, M., Donaldson, D. J., and George, C.: Light changes the atmospheric reactivity of soot, P Natl Acad Sci USA, 107, 6605-6609, 10.1073/pnas.0908341107, 2010.

Ninneman, M., Lu, S., Lee, P., McQueen, J., Huang, J. P., Demerjian, K., and Schwab, J.: Observed and Model-Derived Ozone Production
975   Efficiency over Urban and Rural New York State, Atmosphere-Basel, 8, ARTN 126
10.3390/atmos8070126, 2017.

Nunnermacker, L. J., Kleinman, L. I., Imre, D., Daum, P. H., Lee, Y. N., Lee, J. H., Springston, S. R., Newman, L., and Gillani, N.: NOy lifetimes and O3 production efficiencies in urban and power plant plumes: Analysis of field data, J Geophys Res-Atmos, 105, 9165-9176,
980   Doi 10.1029/1999jd900753, 2000.

Nunnermacker, L. J., Weinstein-Lloyd, J., Kleinman, L., Daum, P. H., Lee, Y. N., Springston, S. R., Klotz, P., Newman, L., Neuroth, G., and Hyde, P.: Ground-based and aircraft measurements of trace gases in Phoenix, Arizona (1998), Atmos Environ, 38, 4941-4956, 10.1016/j.atmosenv.2004.04.033, 2004.
985

Oertel, C., Matschullat, J., Zurba, K., Zimmermann, F., and Erasmi, S.: Greenhouse gas emissions from soils A review, Chemie Der Erde-Geochemistry, 76, 327-352, 10.1016/j.chemer.2016.04.002, 2016.

Olszyna, K. J., Bailey, E. M., Simonaitis, R., and Meagher, J. F.: O3 and NOy relationships at a rural Site, Journal of Geophysical Research-
990   Atmospheres, 99, 14557-14563, Doi 10.1029/94jd00739, 1994.

Osthoff, H. D., Roberts, J. M., Ravishankara, A. R., Williams, E. J., Lerner, B. M., Sommariva, R., Bates, T. S., Coffman, D., Quinn, P. K., Dibb, J. E., Stark, H., Burkholder, J. B., Talukdar, R. K., Meagher, J., Fehsenfeld, F. C., and Brown, S. S.: High levels of nitryl chloride in the polluted subtropical marine boundary layer, Nature Geoscience, 1, 324-328, 2008.

Parrish, D. D., Ryerson, T. B., Mellqvist, J., Johansson, J., Fried, A., Richter, D., Walega, J. G., Washenfelder, R. A., de Gouw, J. A., Peischl, J., Aikin, K. C., McKeen, S. A., Frost, G. J., Fehsenfeld, F. C., and Herndon, S. C.: Primary and secondary sources of formaldehyde in urban atmospheres: Houston Texas region, Atmos Chem Phys, 12, 3273-3288, 10.5194/acp-12-3273-2012, 2012.

Pfannerstill, E. Y., Wang, N. J., Edtbauer, A., Bourtsoukidis, E., Crowley, J. N., Dienhart, D., Eger, P. G., Ernle, L., Fischer, H., Hottmann, B., Paris, J. D., Stonner, C., Tadic, I., Walter, D., and Williams, J.: Shipborne measurements of total OH reactivity around the Arabian Peninsula and its role in ozone chemistry, Atmospheric Chemistry and Physics, 19, 11501-11523, 10.5194/acp-19-11501-2019, 2019.

Platt, U., Perner, D., Harris, G. W., Winer, A. M., and Pitts, J. N.: Observations of Nitrous-Acid in an Urban Atmosphere by Differential Optical-Absorption, Nature, 285, 312-314, DOI 10.1038/285312a0, 1980.

Regelin, E., Harder, H., Martinez, M., Kubistin, D., Ernest, C. T., Bozem, H., Klippel, T., Hosaynali-Beygi, Z., Fischer, H., Sander, R., Jockel, P., Konigstedt, R., and Lelieveld, J.: HOx measurements in the summertime upper troposphere over Europe: a comparison of observations to a box model and a 3-D model, Atmospheric Chemistry and Physics, 13, 10703-10720, 10.5194/acp-13-10703-2013, 2013.

Richter, A., Eyring, V., Burrows, J. P., Bovensmann, H., Lauer, A., Sierk, B., and Crutzen, P. J.: Satellite measurements of NO2 from international shipping emissions, Geophysical Research Letters, 31, Artn L23110 10.1029/2004gl020822, 2004.

Rickard, A. R., Salisbury, G., Monks, P. S., Lewis, A. C., Baugitte, S., Bandy, B. J., Clemitshaw, K. C., and Penkett, S. A.: Comparison of measured ozone production efficiencies in the marine boundary layer at two European coastal sites under different pollution regimes, Journal of Atmospheric Chemistry, 43, 107-134, Doi 10.1023/A:1019970123228, 2002.

Rolph, G., Stein, A., and Stunder, B.: Real-time environmental applications and display system: READY, Environmental Modelling & Software, 95, 210-228, 10.1016/j.envsoft.2017.06.025, 2017.

Romer, P. S., Duffey, K. C., Wooldridge, P. J., Allen, H. M., Ayres, B. R., Brown, S. S., Brune, W. H., Crounse, J. D., de Gouw, J., Draper, D. C., Feiner, P. A., Fry, J. L., Goldstein, A. H., Koss, A., Misztal, P. K., Nguyen, T. B., Olson, K., Teng, A. P., Wennberg, P. O., Wild, R. J., Zhang, L., and Cohen, R. C.: The lifetime of nitrogen oxides in an isoprene-dominated forest, Atmospheric Chemistry and Physics, 16, 7623-7637, 10.5194/acp-16-7623-2016, 2016.

Roussel, P. B., Lin, X., Camacho, F., Laszlo, S., Taylor, R., Melo, O. T., Shepson, P. B., Hastie, D. R., and Niki, H.: Observations of ozone and precursor levels at two sites around Toronto, Ontario, during SONTOS 92, Atmos Environ, 30, 2145-2155, Doi 10.1016/1352-2310(95)00102-6, 1996.

Saxe, H., and Larsen, T.: Air pollution from ships in three Danish ports, Atmospheric Environment, 38, 4057-4067, 10.1016/j.atmosenv.2004.03.055, 2004.

Sillman, S.: Ozone production efficiency and loss of NOx in power plant plumes: Photochemical model and interpretation of measurements in Tennessee, J Geophys Res-Atmos, 105, 9189-9202, Doi 10.1029/1999jd901014, 2000.

Sinha, V., Williams, J., Crowley, J. N., and Lelieveld, J.: The comparative reactivity method - a new tool to measure total OH reactivity in ambient air, Atmospheric Chemistry and Physics, 8, 2213-2227, 2008.

Sobanski, N., Schuladen, J., Schuster, G., Lelieveld, J., and Crowley, J. N.: A five-channel cavity ring-down spectrometer for the detection of NO2, NO3, N2O5, total peroxy nitrates and total alkyl nitrates, Atmospheric Measurement Techniques, 9, 5103-5118, 10.5194/amt-9-5103-2016, 2016.

Stein, A. F., Draxler, R. R., Rolph, G. D., Stunder, B. J. B., Cohen, M. D., and Ngan, F.: NOAA'S HYSPLIT atmospheric transport and dispersion modeling system Bulletin of the American Meteorological Society, 96, 2059-2077, 10.1175/bams-d-14-00110.1, 2015.

Stickler, A., Fischer, H., Williams, J., de Reus, M., Sander, R., Lawrence, M. G., Crowley, J. N., and Lelieveld, J.: Influence of summertime deep convection on formaldehyde in the middle and upper troposphere over Europe, Journal of Geophysical Research-Atmospheres, 111, D14308, doi:10.1029/2005JD007001, 2006.

Stutz, J., Kim, E. S., Platt, U., Bruno, P., Perrino, C., and Febo, A.: UV-visible absorption cross sections of nitrous acid, Journal of Geophysical Research-Atmospheres, 105, 14585-14592, 2000.

Sun, L., Chen, T. S., Jiang, Y., Zhou, Y., Sheng, L. F., Lin, J. T., Li, J., Dong, C., Wang, C., Wang, X. F., Zhang, Q. Z., Wang, W. X., and Xue, L. K.: Ship emission of nitrous acid (HONO) and its impacts on the marine atmospheric oxidation chemistry, Science of the Total Environment, 735, ARTN 139355
10.1016/j.scitotenv.2020.139355, 2020.

Sun, Y., Wang, L. L., Wang, Y. S., Zhang, D. Q., Quan, L., and Xin, J. Y.: In situ measurements of NO, NO2, NOy, and O-3 in Dinghushan (112 degrees E, 23 degrees N), China during autumn 2008, Atmos Environ, 44, 2079-2088, 10.1016/j.atmosenv.2010.03.007, 2010.

Tadic, I., Crowley, J. N., Dienhart, D., Eger, P., Harder, H., Hottmann, B., Martinez, M., Parchatka, U., Paris, J. D., Pozzer, A., Rohloff, R., Schuladen, J., Shenolikar, J., Tauer, S., Lelieveld, J., and Fischer, H.: Net ozone production and its relationship to nitrogen oxides and volatile organic compounds in the marine boundary layer around the Arabian Peninsula, Atmos. Chem. Phys., 20, 6769-6787, 10.5194/acp-20-6769-2020, 2020.

Thieser, J., Schuster, G., Phillips, G. J., Reiffs, A., Parchatka, U., Pöhler, D., Lelieveld, J., and Crowley, J. N.: A two-channel, thermal dissociation cavity-ringdown spectrometer for the detection of ambient NO2, RO2NO2 and RONO2, Atmos. Meas. Tech., 9, 553-576, 10.5194/amt-9-553-2016, 2016.

Trainer, M., Parrish, D. D., Buhr, M. P., Norton, R. B., Fehsenfeld, F. C., Anlauf, K. G., Bottenheim, J. W., Tang, Y. Z., Wiebe, H. A., Roberts, J. M., Tanner, R. L., Newman, L., Bowersox, V. C., Meagher, J. F., Olszyna, K. J., Rodgers, M. O., Wang, T., Berresheim, H., Demerjian, K. L., and Roychowdhury, U. K.: Correlation of Ozone with Noy in Photochemically Aged Air, Journal of Geophysical Research-Atmospheres, 98, 2917-2925, Doi 10.1029/92jd01910, 1993.

Večeřa, Z., Mikuška, P., Smolík, J., Eleftheriadis, K., Bryant, C., Colbeck, I., and Lazaridis, M.: Shipboard Measurements of Nitrogen Dioxide, Nitrous Acid, Nitric Acid and Ozone in the Eastern Mediterranean Sea, Water, Air, & Soil Pollution: Focus, 8, 117-125, 10.1007/s11267-007-9133-y, 2008.

Wang, J. H., Ge, B. Z., and Wang, Z. F.: Ozone Production Efficiency in Highly Polluted Environments, Current Pollution Reports, 4, 198-207, 10.1007/s40726-018-0093-9, 2018.

Wang, T., Carroll, M. A., Albercook, G. M., Owens, K. R., Duderstadt, K. A., Markevitch, A. N., Parrish, D. D., Holloway, J. S., Fehsenfeld, F. C., Forbes, G., and Ogren, J.: Ground-based measurements of NOx and total reactive oxidized nitrogen (NOy) at Sable Island, Nova Scotia, during the NARE 1993 summer intensive, Journal of Geophysical Research-Atmospheres, 101, 28991-29004, Doi 10.1029/96jd01090, 1996.

Wild, R. J., Edwards, P. M., Dube, W. P., Baumann, K., Edgerton, E. S., Quinn, P. K., Roberts, J. M., Rollins, A. W., Veres, P. R., Warneke, C., Williams, E. J., Yuan, B., and Brown, S. S.: A measurement of total reactive nitrogen, NOy, together with NO2, NO, and O3 via cavity ring-down spectroscopy, Environmental Science & Technology, 48, 9609-9615, doi:10.1021/es501896w, 2014.

Wild, R. J., Edwards, P. M., Bates, T. S., Cohen, R. C., de Gouw, J. A., Dube, W. P., Gilman, J. B., Holloway, J., Kercher, J., Koss, A. R., Lee, L., Lerner, B. M., McLaren, R., Quinn, P. K., Roberts, J. M., Stutz, J., Thornton, J. A., Veres, P. R., Warneke, C., Williams, E., Young, C. J., Yuan, B., Zarzana, K. J., and Brown, S. S.: Reactive nitrogen partitioning and its relationship to winter ozone events in Utah, Atmospheric Chemistry and Physics, 16, 573-583, 10.5194/acp-16-573-2016, 2016.

Williams, E. J., Lerner, B. M., Murphy, P. C., Herndon, S. C., and Zahniser, M. S.: Emissions of NOx, SO2, CO, and HCHO from commercial marine shipping during Texas Air Quality Study (TexAQS) 2006, Journal of Geophysical Research-Atmospheres, 114, Artn D21306
10.1029/2009jd012094, 2009.

Wojtal, P., Halla, J. D., and McLaren, R.: Pseudo steady states of HONO measured in the nocturnal marine boundary layer: a conceptual model for HONO formation on aqueous surfaces, Atmos Chem Phys, 11, 3243-3261, 10.5194/acp-11-3243-2011, 2011.

1105 Wolfe, G. M., Kaiser, J., Hanisco, T. F., Keutsch, F. N., de Gouw, J. A., Gilman, J. B., Graus, M., Hatch, C. D., Holloway, J., Horowitz, L. W., Lee, B. H., Lerner, B. M., Lopez-Hilifiker, F., Mao, J., Marvin, M. R., Peischl, J., Pollack, I. B., Roberts, J. M., Ryerson, T. B., Thornton, J. A., Veres, P. R., and Warneke, C.: Formaldehyde production from isoprene oxidation across NOx regimes, Atmos. Chem. Phys., 16, 2597-2610, 10.5194/acp-16-2597-2016, 2016.

1110 Wolfe, G. M., Nicely, J. M., St. Clair, J. M., Hanisco, T. F., Liao, J., Oman, L. D., Brune, W. B., Miller, D., Thames, A., González Abad, G., Ryerson, T. B., Thompson, C. R., Peischl, J., McKain, K., Sweeney, C., Wennberg, P. O., Kim, M., Crounse, J. D., Hall, S. R., Ullmann, K., Diskin, G., Bui, P., Chang, C., and Dean-Day, J.: Mapping hydroxyl variability throughout the global remote troposphere via synthesis of airborne and satellite formaldehyde observations, Proceedings of the National Academy of Sciences, 116, 11171-11180, 10.1073/pnas.1821661116, 2019.

1115 Womack, C. C., Neuman, J. A., Veres, P. R., Eilerman, S. J., Brock, C. A., Decker, Z. C. J., Zarzana, K. J., Dube, W. P., Wild, R. J., Wooldridge, P. J., Cohen, R. C., and Brown, S. S.: Evaluation of the accuracy of thermal dissociation CRDS and LIF techniques for atmospheric measurement of reactive nitrogen species, Atmospheric Measurement Techniques, 10, 1911-1926, 10.5194/amt-10-1911-2017, 2017.

1120 Wood, E. C., Herndon, S. C., Onasch, T. B., Kroll, J. H., Canagaratna, M. R., Kolb, C. E., Worsnop, D. R., Neuman, J. A., Seila, R., Zavala, M., and Knighton, W. B.: A case study of ozone production, nitrogen oxides, and the radical budget in Mexico City, Atmospheric Chemistry and Physics, 9, 2499-2516, 10.5194/acp-9-2499-2009, 2009.

Wu, D., Hu, Y. X., McCormick, M. P., Xu, K. M., Liu, Z. Y., Smith, B., Omar, A. H., and Chang, F. L.: Deriving Marine-Boundary-Layer
1125 Lapse Rate from Collocated CALIPSO, MODIS, and AMSR-E Data to Study Global Low-Cloud Height Statistics, Ieee Geoscience and Remote Sensing Letters, 5, 649-652, 10.1109/Lgrs.2008.2002024, 2008.

Ye, C. X., Zhou, X. L., Pu, D., Stutz, J., Festa, J., Spolaor, M., Tsai, C., Cantrell, C., Mauldin, R. L., Campos, T., Weinheimer, A., Hornbrook, R. S., Apel, E. C., Guenther, A., Kaser, L., Yuan, B., Karl, T., Haggerty, J., Hall, S., Ullmann, K., Smith, J. N., Ortega, J., and Knote, C.:
1130 Rapid cycling of reactive nitrogen in the marine boundary layer, Nature, 532, 489-491, 10.1038/nature17195, 2016.

Zorn, S. R., Drewnick, F., Schott, M., Hoffmann, T., and Borrmann, S.: Characterization of the South Atlantic marine boundary layer aerosol using an aerodyne aerosol mass spectrometer, Atmospheric Chemistry and Physics, 8, 4711-4728, 10.5194/acp-8-4711-2008, 2008.

1135
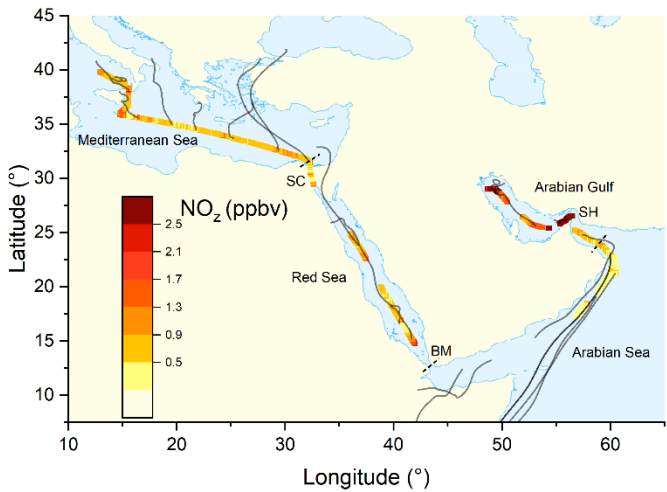
Figure 1: Mixing ratio of NO$_z$ from the second leg of the campaign, colour-coded along the ship track. Each data point represents an average over 30 minutes. Grey lines represent HYSPLIT 48 hours back trajectories starting from the ship location at 100 m height. SH = Strait of Hormuz; BM = Strait of Bab al-Mandab; SC = Suez Canal.
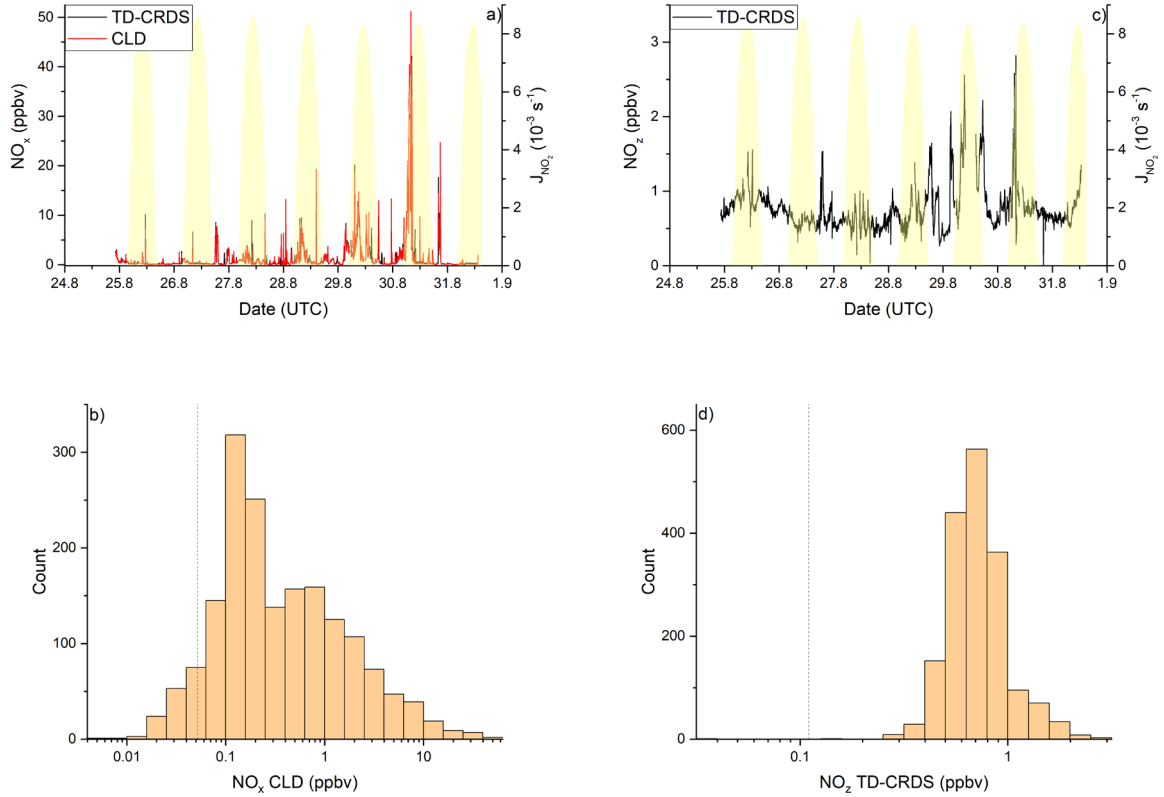
Figure 2: NO_y measurements in the *Mediterranean Sea*. Dashed lines signify the instrument detection limits. *(a)* NO_x mixing ratios by CLD and TD-CRDS. *(b)* Frequency distribution of NO_x mixing ratios between 25 August and 1 September 2017. *(c)* NO_z mixing ratios by TD-CRDS. *(d)* Frequency distribution of NO_z mixing ratios between 25 August and 1 September 2017. The yellow shaded regions show J_{NO2}. The vertical dotted lines are the limits of detection of the respective measurements.
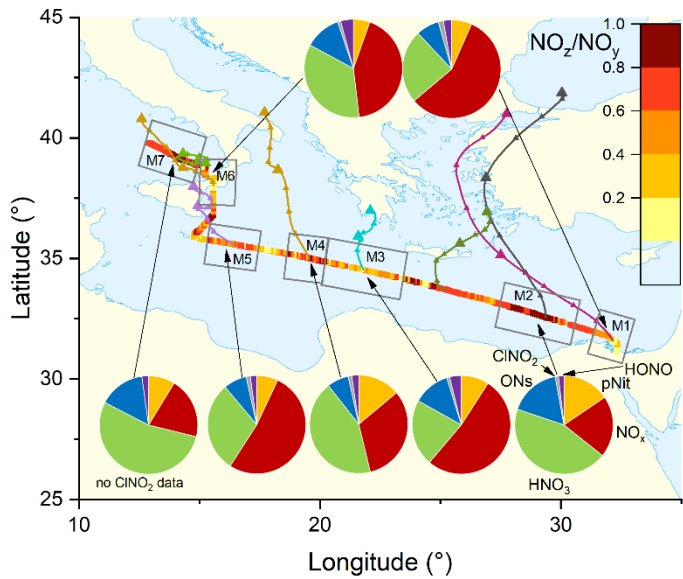
Figure 3: The NO_z / NO_y ratio over the *Mediterranean Sea*. Coloured lines are 2-day back-trajectories (HYSPLIT). The pie charts indicate the components of NO_y at various segments along the ship's track (ONs = organic nitrates, pNit = particulate nitrate). HNO_3 was calculated via: $HNO_3 = NO_z - (ONs + pNit + NO_x + ClNO_2 + HONO)$. The colours of the pie chart segments are assigned as follows (clockwise): pNit in yellow, NO_x in red, HNO_3 in green, ONs in blue, $ClNO_2$ in grey, and HONO in magenta.
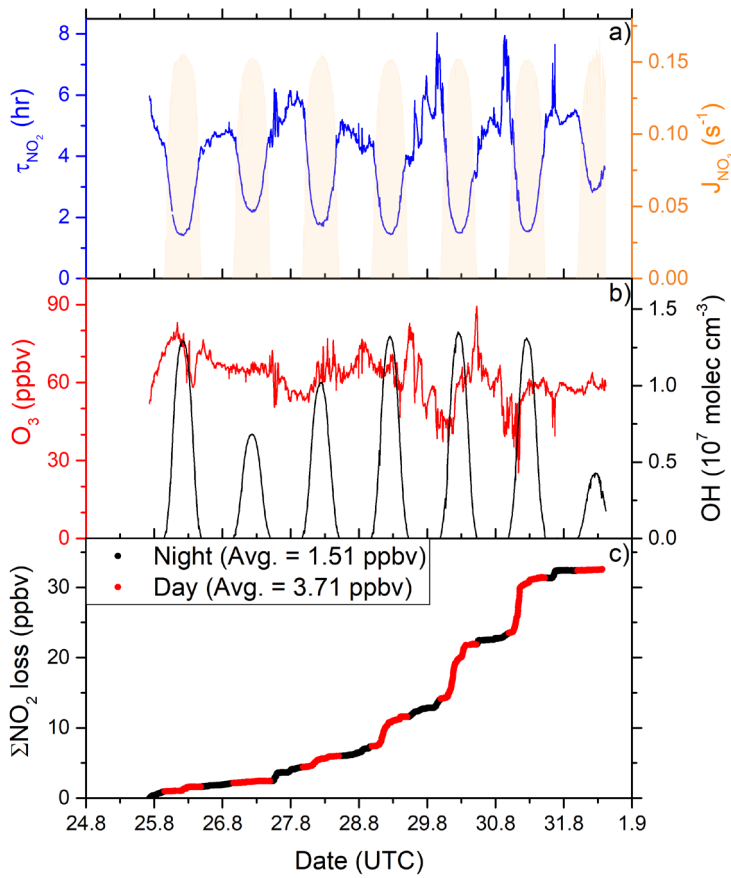
Figure 4: *(a)* Lifetime (τ) of NO_2 due to reactions with OH and O_3 in the *Mediterranean Sea*, together with concentrations of O_3 and OH. The OH trace is an interpolation based on OH measurements and J_{O1D} (see Sect. 3.1.3). Daytime hours are indicated via J_{NO3}. *(b)* Cumulative loss of NO_2 during the displayed time frame, based on the calculated lifetimes and measured NO_2.
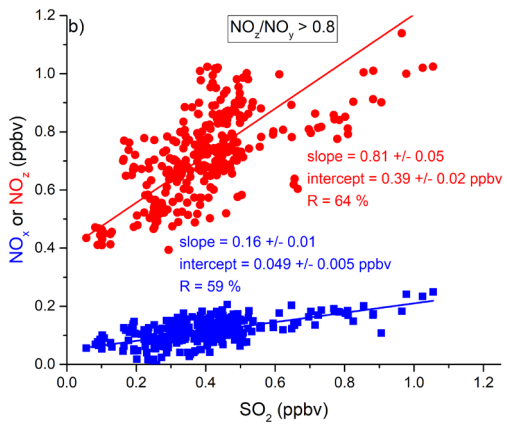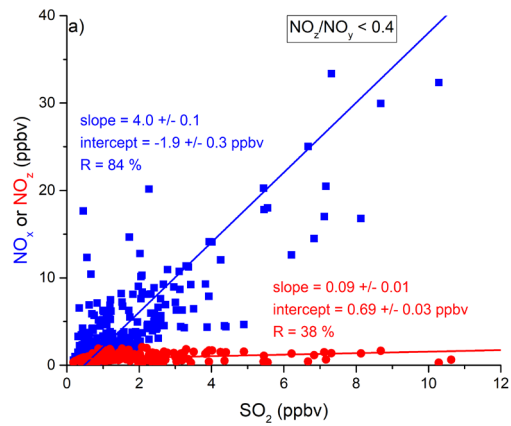
Figure 5: Correlation between SO_2 and NO_x or NO_z for *(a)* fresh and *(b)* aged NO_x emissions in the *Mediterranean Sea*.
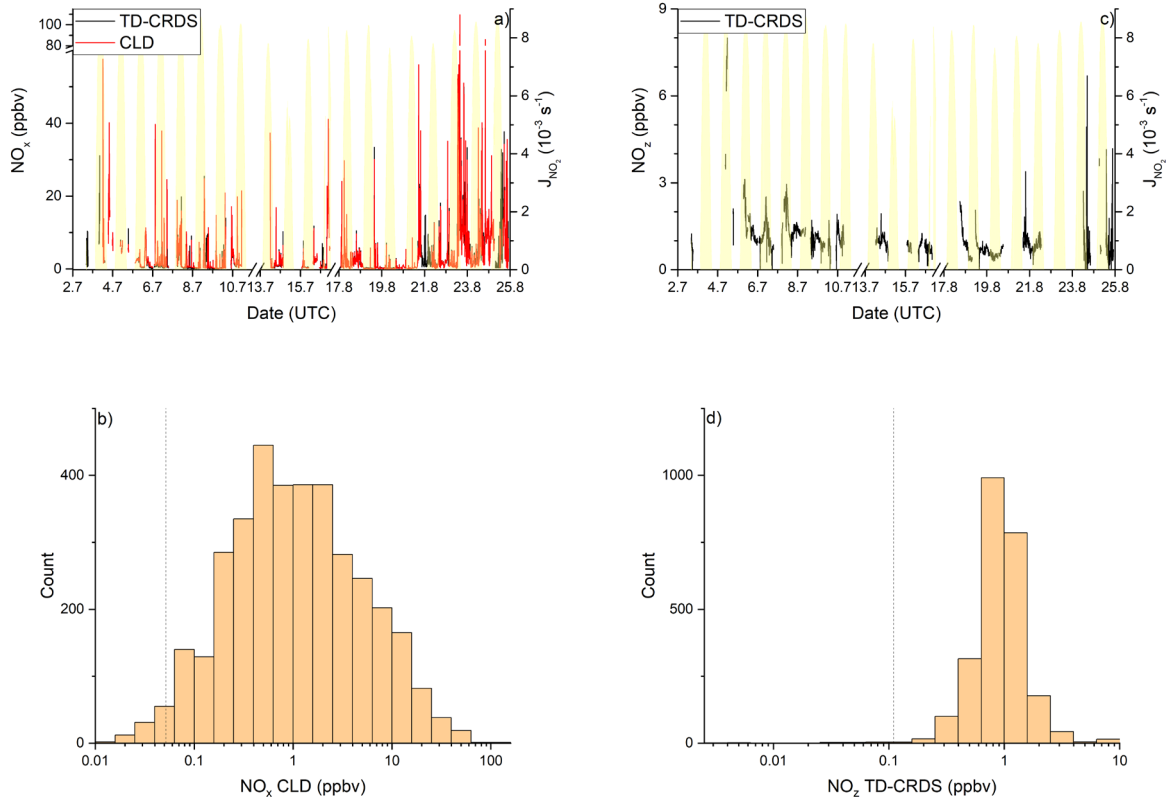
Figure 6: NO_y measurements in the *Red Sea*. Dashed lines signify the instrument detection limits. *(a)* NO_x mixing ratios by CLD and TD-CRDS. *(b)* Frequency distribution of NO_x mixing ratios during 2.-16.7.2017 and 17.-24.8.2017, excluding the layover in Jeddah. *(c)* NO_z mixing ratios by TD-CRDS. *(d)* Frequency of NO_z mixing ratios during 2.-16.7.2017 and 17.-24.8.2017. The yellow shaded regions show J_{NO2}. The vertical dotted lines are the limits of detection of the respective measurements.
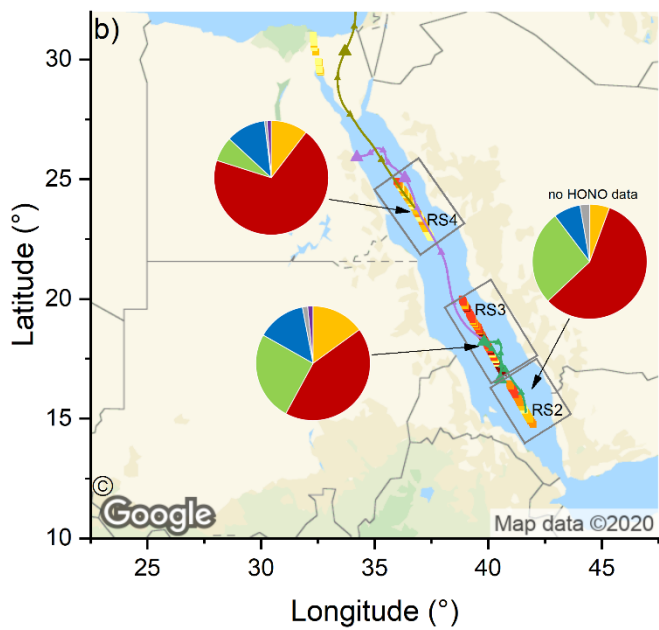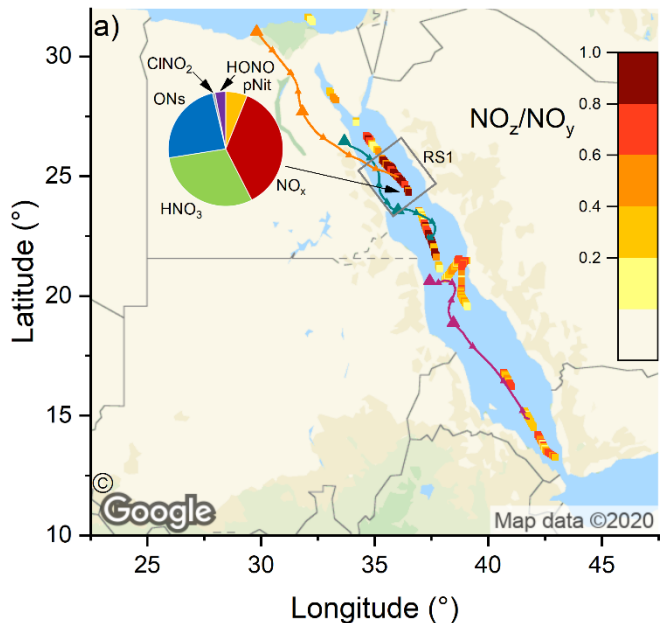
Figure 7: The NO_z / NO_y ratio over the Red Sea during the *(a)* first and *(b)* second leg. Coloured lines are 2-day back-trajectories (HYSPLIT). The pie charts indicate the components of NO_y at various segments along the ship's track (ONs = organic nitrates, pNit = particulate nitrate). HNO_3 was calculated via: $HNO_3 = NO_z - (ONs + pNit + NO_x + ClNO_2 + HONO)$.

The colours of the pie chart segments are assigned as follows (clockwise): pNit in yellow, NO_x in red, HNO_3 in green, ONs in blue, $ClNO_2$ in grey, and HONO in magenta.
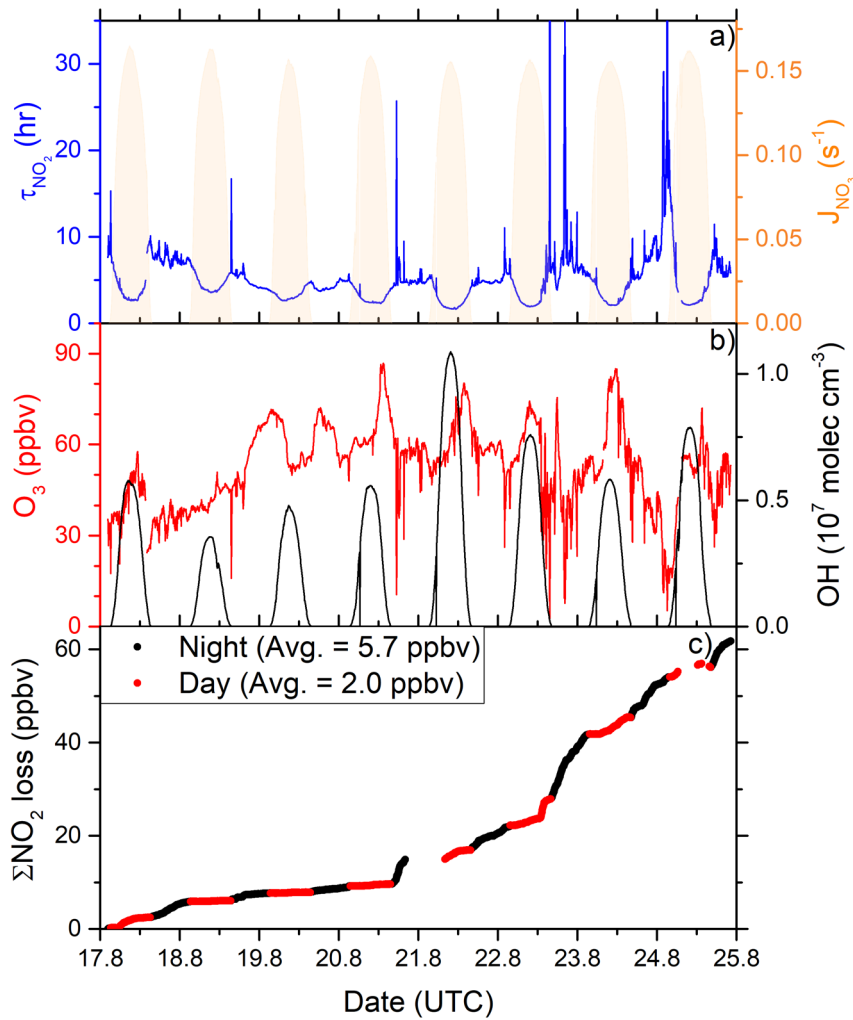
Figure 8: *(a)* Lifetime (τ) of NO_2 due to reactions with OH and O_3 along the second *Red Sea* leg, together with concentrations of O_3 and OH. The OH trace is an interpolation based on OH measurements and J_{O1D} (see Sect. 3.2.3). Daytime hours are indicated via J_{NO3}. *(b)* Cumulative loss of NO_2 during the displayed time frame, based on the calculated lifetimes and measured NO_2.
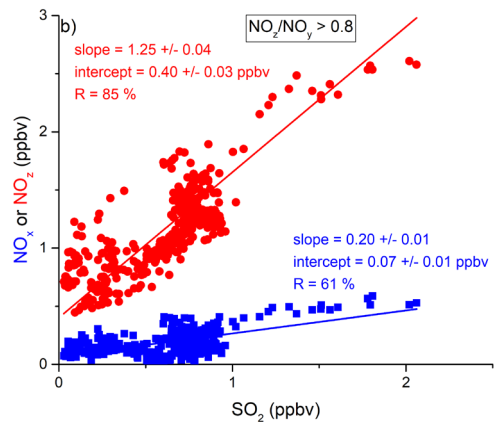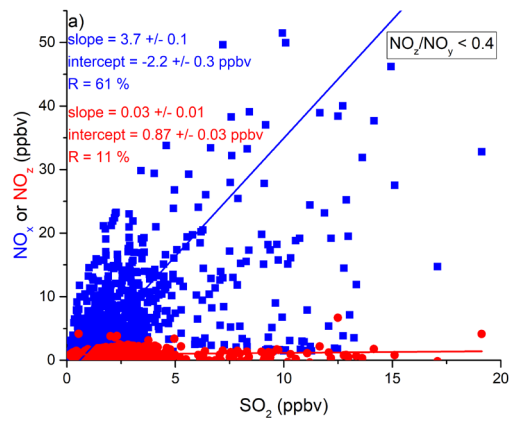
Figure 9: Correlation between SO_2 and NO_x or NO_z for *(a)* fresh and *(b)* aged NO_x emissions in the *Red Sea*.
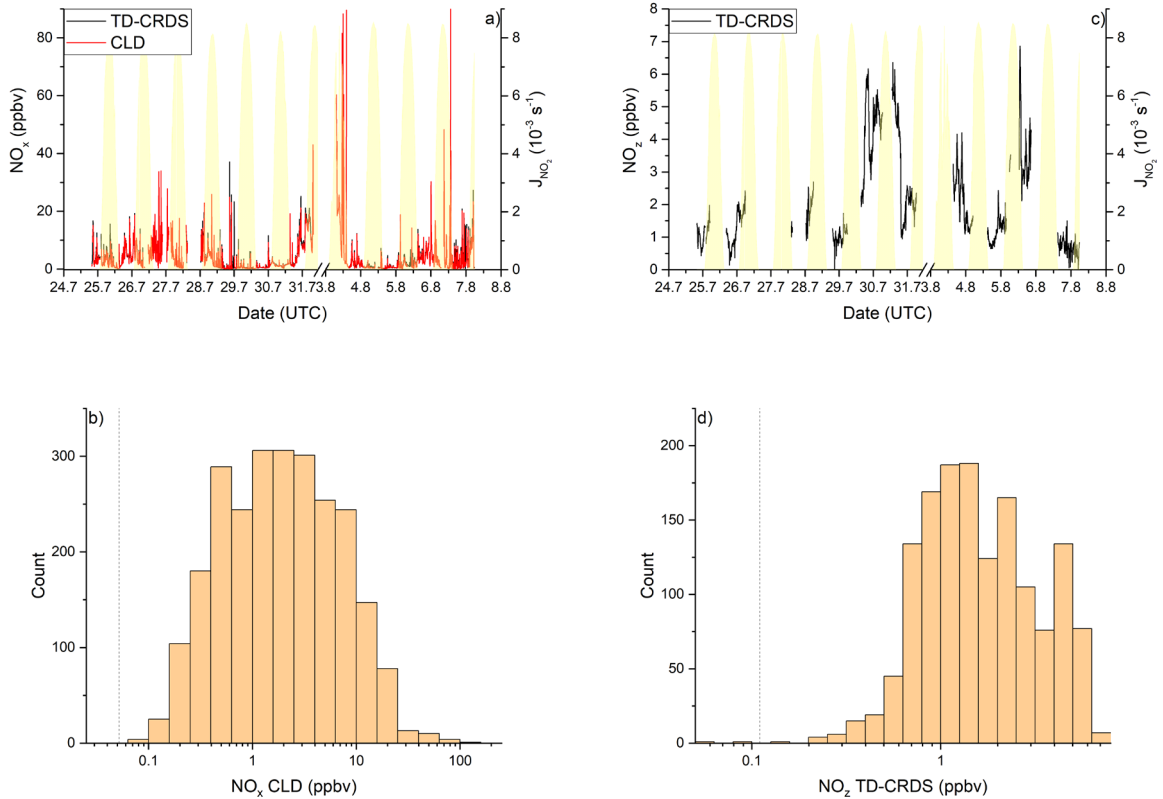
Figure 10: NO_y measurements in the *Arabian Gulf*. Dashed lines signify the instrument detection limits. *(a)* NO_x mixing ratios by CLD and TD-CRDS. The NO_x peak in the afternoon of 6.8.2017 reached 153 ppbv. *(b)* Frequency of NO_x mixing ratios between 24.7. and 7.8.2017, excluding the layover in Kuwait. *(c)* NO_z mixing ratios by TD-CRDS. *(d)* Frequency of NO_z mixing ratios between 24.7. and 7.8.2020. The yellow shaded regions show J_{NO2}.
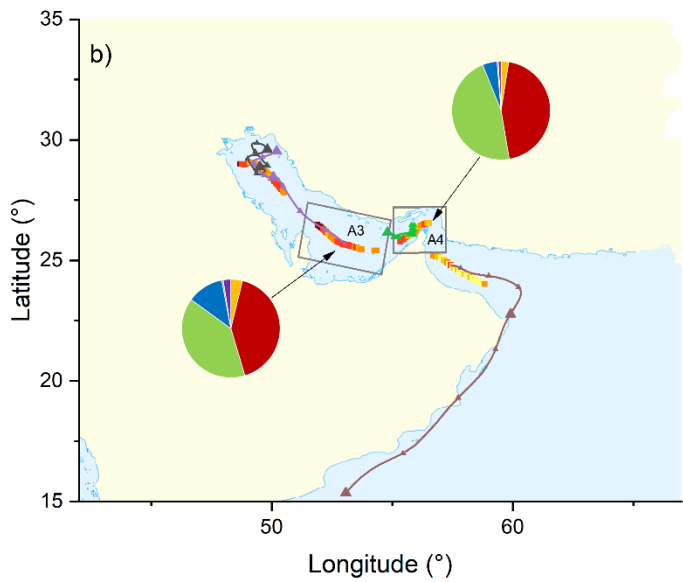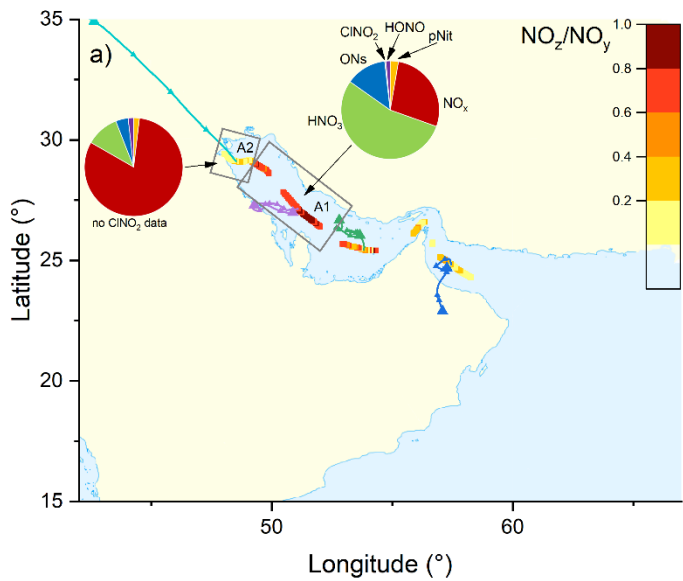
Figure 11: The NO_z / NO_y ratio over the Arabian Gulf during the *(a)* first and *(b)* second leg. Coloured lines are 2-day back-trajectories (HYSPLIT). The pie charts indicate the components of NO_y at various segments along the ship's track (ONs = organic nitrates, pNit = particulate nitrate). HNO_3 was calculated via: $HNO_3 = NO_z - (ONs + pNit + NO_x + ClNO_2 + HONO)$.

The colours of the pie chart segments are assigned as follows (clockwise): pNit in yellow, NO_x in red, HNO_3 in green, ONs in blue, $ClNO_2$ in grey, and HONO in magenta.
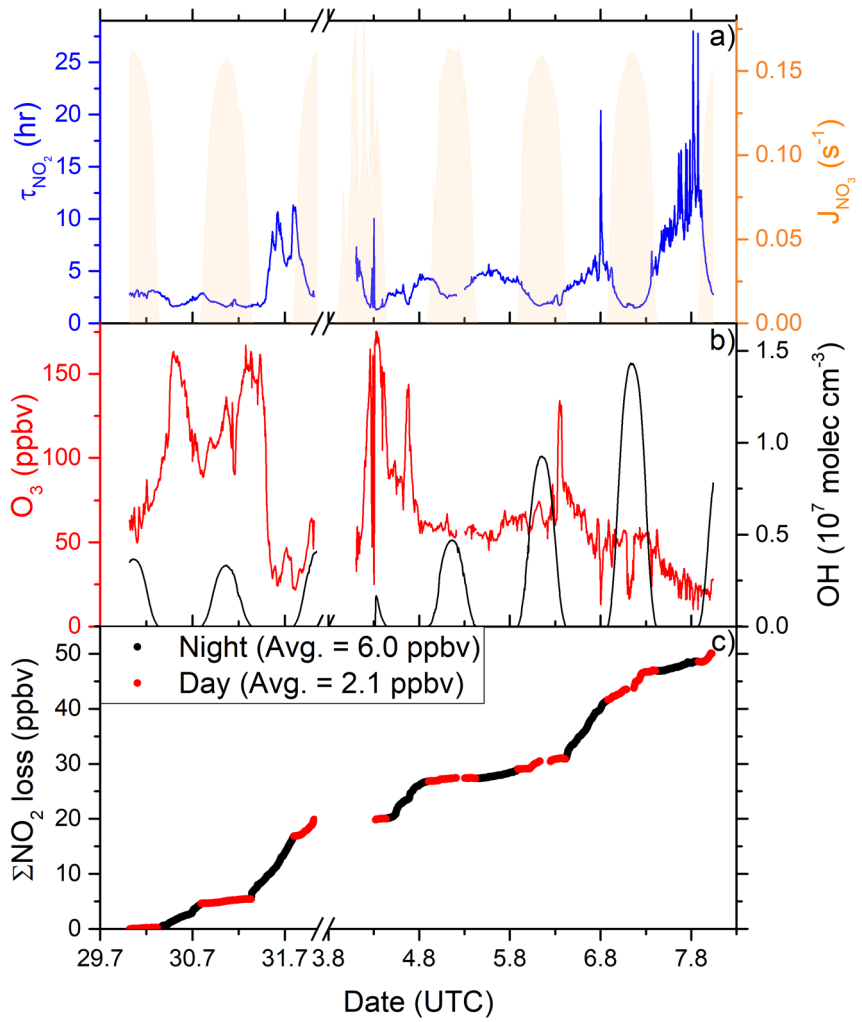
Figure 12: *(a)* Lifetime (τ) of NO_2 due to reactions with OH and O_3 in the *Arabian Gulf*, together with concentrations of O_3 and OH. The OH trace is an interpolation based on OH measurements and J_{O1D} (see Sect. 3.3.3). Daytime hours are indicated via J_{NO3}. *(b)* Cumulative loss of NO_2 during the displayed time frame, based on the calculated lifetimes and measured NO_2.
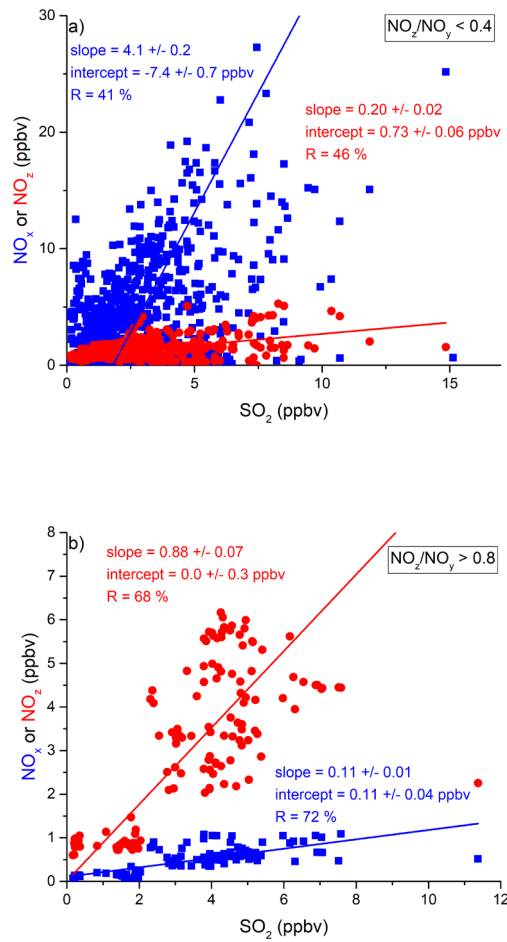
Figure 13: Correlation between SO_2 and NO_x or NO_z for *(a)* fresh and *(b)* aged NO_x emissions in the *Arabian Gulf*.
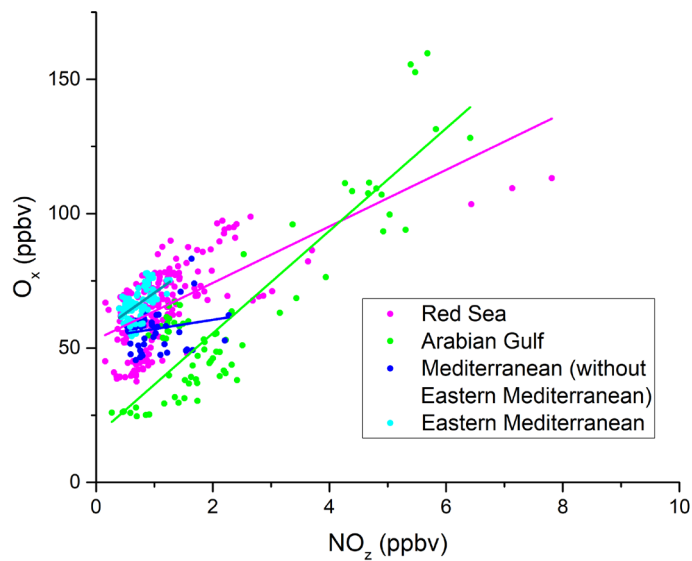
Figure 14: Correlation between O_x (= O_3 + NO_2) and NO_z during AQABA, with the regions indicated via the colour code. Only daytime measurements were used in this analysis. The OPEs for AQABA and for the individual regions shown in Table 4 were derived from linear fits of these data points. A clear regional variability can be observed for O_x and NO_z mixing ratios. Elevated O_x and NO_z levels were measured in the Arabian Gulf and the Red Sea.
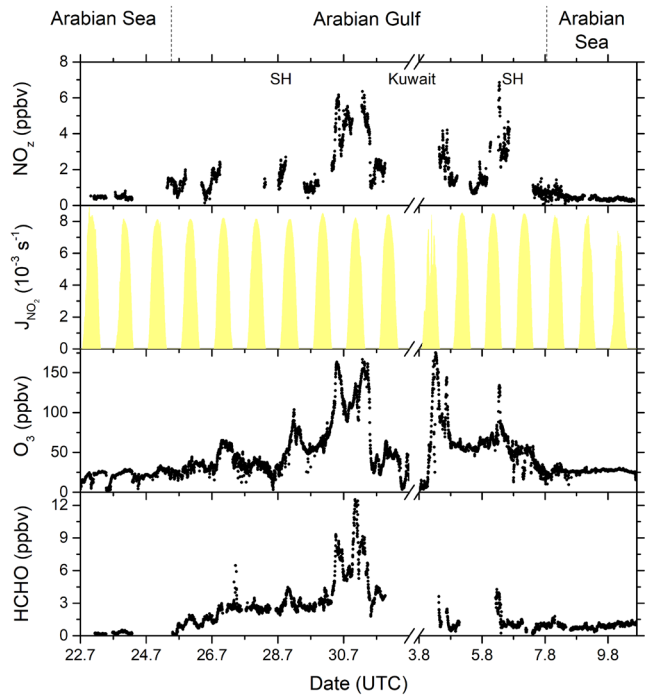
Figure 15: NO$_z$, O$_3$ and HCHO mixing ratios, together with NO$_2$ photolysis rates, during the transitions between the Arabian Sea and Gulf, and in the Arabian Gulf.

Table 1: Data sets used in the analysis and corresponding measurement characteristics.

Species	Instrument	Technique	Detection limit	Measurement uncertainty
NO_x	TD-CRDS	thermal dissociation cavity-ringdown-spectroscopy	98 pptv	11 %
NO_z			110 pptv	16 %
NO	CLD	chemiluminescence	22 pptv (5s, 2σ)	6 %
NO_2			52 pptv (5s, 2σ)	23 %
ONs	5C-TD-CRDS	thermal dissociation cavity-ringdown-spectroscopy	n/a	n/a
SO_2	CI-QMS	chemical ionization mass spectrometry	38 pptv	20 % ± 23 pptv
$ClNO_2$			12 pptv	30 % ± 6 pptv
pNit (PM_1)	AMS	aerosol mass spectrometry	n/a	30 %
SO_4^{2-} (PM_1)			n/a	35 %
PM_1*	OPC	optical particle counter	n/a	35 %
PM_{10}*				
O_3	O_3	optical absorption	3 ppbv (10 s)	2 % ± 1 ppbv
HONO	LOPAP	long path absorption photometry	3-5 pptv	20 %
J_x**	J_x	wavelength resolved actinic flux	n/a	10 %
OH	LIF	laser induced fluorescence	variable	40 % (upper limit)
OH reactivity	OH reactivity	comparative reactivity method	5.4 s^{-1} (5 min)	ca. 50 %
HCHO	HCHO	Hantzsch method	0.128 ppbv (170 s, 2σ)	13 %
CO	CO	absorption spectroscopy with quantum-cascade-laser	0.6 ppbv	20 %

* = total aerosol mass concentration; ** = photolysis rate constants for NO_2, NO_3 and HONO

Table 2: Summary of correlation results between NO_x/NO_z and SO_2 in all regions.

Region	NO_z / NO_y	Species	Slope	Intercept (ppbv)	R (%)
Mediterranean Sea	< 0.4	NO_x	4.0 ± 0.1	-1.9 ± 0.3	84
		NO_z	0.09 ± 0.01	0.69 ± 0.03	38
	> 0.8	NO_x	0.16 ± 0.01	0.049 ± 0.005	59
		NO_z	0.81 ± 0.05	0.39 ± 0.02	64
Red Sea	< 0.4	NO_x	3.7 ± 0.1	-2.2 ± 0.3	61
		NO_z	0.03 ± 0.01	0.87 ± 0.03	11
	> 0.8	NO_x	0.20 ± 0.01	0.07 ± 0.01	61
		NO_z	1.25 ± 0.04	0.40 ± 0.03	85
Arabian Gulf	< 0.4	NO_x	4.1 ± 0.2	-7.4 ± 0.7	41
		NO_z	0.20 ± 0.02	0.73 ± 0.06	46
	> 0.8	NO_x	0.11 ± 0.01	0.11 ± 0.04	72
		NO_z	0.88 ± 0.07	0.0 ± 0.3	68

Table 3: Average required production rates to maintain the observed NO_x mixing ratios in aged air masses during the *Mediterranean Sea* transit and contributions from processes R12-R14.

	Mediterranean Sea
$P_{chem} \pm SD$ (10^5 molec cm^{-3} s^{-1})	2.8 ± 2.2
$P(HONO+h\nu) \pm SD$ (10^5 molec cm^{-3} s^{-1})	13.1 ± 9.1
$P(pNit+h\nu) \pm SD$ (10^5 molec cm^{-3} s^{-1})	1.8 ± 0.4
$P(OH+HNO_3) \pm SD$ (10^5 molec cm^{-3} s^{-1})	0.14 ± 0.06
Number of data points (5 min averages)	90

Table 4: Ozone production efficiencies (OPEs) for AQABA and the individual regions.

	AQABA	Eastern Med. Sea	Red Sea	Arabian Gulf
OPE	14.1 ± 0.7	15.4 ± 2.4	10.5 ± 0.9	19.1 ± 1.1
Correlation Coeff. R (%)	65	55	65	89
$k_{NO_x}^{OH} / k_{total}^{OH}$ (%) [a]		1.0	2.0	7.5
O_3 (ppbv) [b]		58-73	42-81	23-108
NO_z (ppbv) [b]		0.5-1.0	0.5-2.1	0.9-4.9
NO_y / CO (%) [b,c]			1.4-7.0	1.9-14.6
OH_{max} (10^6 molec cm^{-3}) [d]		9.1	5.7	11.8

(a) Median
(b) 10 – 90 percentiles
(c) No CO data after 16 August 2017
(d) Average of daily OH peak concentrations, no data before 18 July 2017